Journal of Hydrology 524 (2015) 680–695

Contents lists available at ScienceDirect

Journal of Hydrology

journal homepage: www.elsevier.com/locate/jhydrol

Imaging and characterization of facies heterogeneity in an alluvial aquifer using GPR full-waveform inversion and cone penetration tests

Nils Gueting [a,*], Anja Klotzsche [a,b], Jan van der Kruk [a,b], Jan Vanderborght [a,b], Harry Vereecken [a,b], Andreas Englert [c]

[a] Agrosphere Institute, IBG-3, Forschungszentrum Jülich GmbH, 52428 Jülich, Germany
[b] Centre for High-Performance Scientific Computing in Terrestrial Systems (TerrSys), Germany
[c] Earth Sciences Department, Ruhr University Bochum, 44801 Bochum, Germany

ARTICLE INFO

Article history:
Received 20 October 2014
Received in revised form 12 March 2015
Accepted 13 March 2015
Available online 21 March 2015
This manuscript was handled by Peter K. Kitanidis, Editor-in-Chief, with the assistance of Niklas Linde, Associate Editor

Keywords:
Heterogeneity
Aquifer characterization
Geophysical methods
Ground penetrating radar
Full-waveform inversion
Cone penetration tests

SUMMARY

Spatially highly resolved mapping of aquifer heterogeneities is critical for the accurate prediction of groundwater flow and contaminant transport. Here, we demonstrate the value of using full-waveform inversion of crosshole ground penetrating radar (GPR) data for aquifer characterization. We analyze field data from the Krauthausen test site, where crosshole GPR data were acquired along a transect of 20 m length and 10 m depth. Densely spaced cone penetration tests (CPT), located close to the GPR transect, were used to validate and interpret the tomographic images obtained from GPR. A strong correlation was observed between CPT porosity logs and porosity estimates derived from GPR using the Complex Refractive Index Model (CRIM). A less pronounced correlation was observed between electrical conductivity data derived from GPR and CPT. Cluster analysis of the GPR data defined three different subsurface facies, which were found to correspond to sediments with different grain size and porosity. In conclusion, our study suggests that full-waveform inversion of crosshole GPR data followed by cluster analysis is an applicable approach to identify hydrogeological facies in alluvial aquifers and to map their architecture and connectivity. Such facies maps provide valuable information about the subsurface heterogeneity and can be used to construct geologically realistic subsurface models for numerical flow and transport prediction.

1. Introduction

Reliable prediction of groundwater flow and solute transport is needed for environmental engineering tasks such as the definition of protection zones for drinking water wells or the development of efficient remediation strategies at contaminated sites. However, predicting subsurface flow and transport is challenging due to the complex heterogeneity found in most geologic media. Physical and chemical properties in the subsurface vary over orders of magnitude and their spatial variability exerts a primary control on groundwater flow and solute migration (e.g. Dagan, 1989). Sedimentary deposits, which commonly represent soils and aquifers, are often composed of several distinct units or facies, separated by recognizable boundaries at which subsurface properties such as grain size or hydraulic conductivity may abruptly change (Miall, 1985; Fogg, 1986; Koltermann and Gorelick, 1996). This has motivated the conceptualization of heterogeneous sedimentary aquifers as assemblages of distinct (hydro-)lithological facies with less variability within than between facies (Anderson, 1989; Webb and Anderson, 1996; Barrash and Clemo, 2002; Riva et al., 2006; Bayer et al., 2011).

Field and modeling studies have highlighted the influence of facies architecture and geometry on flow and transport processes (Zheng and Gorelick, 2003; Feyen and Caers, 2006; Ronayne et al., 2008; Zheng et al., 2011; Haendel and Dietrich, 2012). In particular, the spatial connectivity of facies appears to be of substantial importance, because connected structures of high permeability act as preferential flow paths and lead to increased water fluxes and increased transport velocities, while connected structures of low permeability act as flow barriers and lead to decreased water fluxes and decreased transport velocities (Zinn and Harvey, 2003; Knudby and Carrera, 2006; Huysmans and Dassargues, 2009; Bianchi et al., 2011; Renard and Allard, 2013). Hence, reliable prediction of flow and transport in the subsurface critically depends on a detailed characterization of the spatial distribution of subsurface facies.

* Corresponding author. Tel.: +49 2461 61 8663.
E-mail address: n.gueting@fz-juelich.de (N. Gueting).

http://dx.doi.org/10.1016/j.jhydrol.2015.03.030
0022-1694/

Unfortunately, a detailed characterization of the subsurface is difficult to obtain in practice because the subsurface is not easily accessible through measurements. Conventional subsurface characterization techniques tend to rely on pumping tests or borehole based geophysical or lithological logs. Pumping tests yield appropriate upscaled properties with regard to flow but suffer from a limited spatial resolution of local properties, which are needed for proper transport prediction. Borehole logs provide detailed information about the vertical distribution of local properties but are inherently one-dimensional in nature. Any inference based on one-dimensional vertical profiles, will be blind to the lateral distribution of subsurface properties, and thus, the interconnectivity of facies. Outcrop analyses can be applied to map the distribution of facies on outcrop walls, which provides valuable information about the lateral connection of facies (Huysmans et al., 2008; Huysmans and Dassargues, 2009; Bayer et al., 2011; Comunian et al., 2011). However, the characteristics derived from an outcrop are not necessarily valid for the specific conditions at locations some distance away from the outcrop.

In contrast, minimally invasive tomographic geophysical imaging methods such as crosshole ground penetrating radar (GPR) can be used to map the spatial distribution of subsurface properties on full cross-sections directly at the location of interest. The two-dimensionality of the tomographic images provides the opportunity to characterize the lateral distribution of structures and to evaluate their architecture and connectivity. Traditional tomographic inversion of GPR data is carried out using ray-based techniques (Holliger et al., 2001; Maurer and Musil, 2004). Because ray-based methods consider only the first arrival times and the first-cycle amplitudes they exploit only a limited amount of the information contained in the full recorded waveform. As a consequence, the spatial resolution of such methods is limited, and only relatively smooth images of the subsurface can be obtained (Belina et al., 2009; Klotzsche et al., 2010). In contrast, full-waveform inversion techniques make use of the full recorded waveform, which includes information beyond the first arrival times and first-cycle amplitudes. As a consequence, full-waveform inversion techniques are capable to resolve subsurface properties with higher spatial resolution and yield tomographic images with a significantly improved level of detail (Ernst et al., 2007b; Meles et al., 2010; Yang et al., 2013; Klotzsche et al., 2013, 2014).

Recent studies showed the potential of GPR full-waveform tomography for hydrogeological application by comparing GPR results with independent measurements of porosity (Yang et al., 2013; Klotzsche et al., 2013) and hydraulic conductivity (Klotzsche et al., 2013). Within the scope of hydrogeological site characterization the strength of full-waveform GPR tomography lies in its potential to bridge the gap in terms of resolution and coverage that exists among traditional hydrogeological methods such as small-scale core analyses and large-scale pumping tests. However, this advantage comes along with difficulties regarding the hydrogeological interpretation because GPR returns the electrical properties which are only indirectly related to hydrogeological parameters such as porosity or hydraulic conductivity. Without information about the site-specific relationship between electrical and hydrogeological properties, the use of GPR for hydrogeological site characterization can therefore be limited. Another difficulty, in field applications, is to evaluate the reliability of the obtained tomographic images, because in the absence of secondary information it is difficult to validate if the structures seen in the tomographic images represent real subsurface structures and not inversion artifacts.

In the present study we show the value of applying full-waveform GPR tomography in combination with complementary investigation tools to hydrogeologically characterize a site. We analyze field data from the Krauthausen test site, where GPR data were recently acquired along several cross-borehole planes. Because the Krauthausen test site has been intensively investigated in previous studies (e.g. Vereecken et al., 2000; Tillmann et al., 2008), we are able to confront the GPR results with densely spaced secondary data from cone penetration tests (CPT), grain size analyses and flowmeter measurements which allow detailed validation and interpretation of the tomographic images obtained from GPR. In detail, our approach consists of the following steps: Firstly, a GPR full-waveform inversion is applied to infer the subsurface permittivity and electrical conductivity distribution along a vertical aquifer cross-section of approximately 20 m length and 10 m depth. Results are validated by comparison with co-located CPT porosity and electrical conductivity logs. Secondly, a cluster analysis is conducted to partition the obtained GPR tomographic images into clusters. In this way, different lithological facies such as sand and gravel that differ in their permittivity and electrical conductivity signatures can be distinguished. The outcome of the cluster analysis is a cross-sectional map showing the spatial distribution of different facies in the aquifer. We discuss the reliability of the facies classification by comparing the distribution of facies obtained from GPR with the distribution of facies obtained independently from CPT. Finally, we use the combined information from GPR, CPT, grain size analyses and flowmeter measurements to develop a hydrogeological interpretation of the obtained facies and to characterize them in terms of grain size, porosity and hydraulic conductivity.

2. Material and methods

2.1. Study site

The Krauthausen test site, set up by the research center Jülich in 1993, is located approximately 10 km northwest of the city of Düren, Germany, in the southern part of the Lower Rhine Embayment. A detailed description of the test site is given by Vereecken et al. (2000). In the last decades, several laboratory and field techniques have been applied at Krauthausen with the goal to study the spatial distribution of aquifer parameters and its effect on solute migration. These techniques include laboratory characterization of sediment samples (Döring, 1997), field pumping and flowmeter tests (Li et al., 2007, 2008) tracer experiments (Vereecken et al., 2000; Vanderborght and Vereecken, 2001), geophysical imaging methods (Kemna et al., 2002; Müller et al., 2010; Oberröhrmann et al., 2013), and cone penetration tests (Tillmann et al., 2008). Due to the extensive set of subsurface information retrieved in previous studies, Krauthausen provides excellent opportunities to test and validate novel aquifer exploration techniques.

The present study focuses on the uppermost aquifer in the central part of the test site where a series of closely spaced boreholes and cone penetration tests were available (Fig. 1). The unconfined aquifer is approximately 10 m thick and composed of alluvial terrace sediments, which were deposited by a local braided river system of the river Rur on top of older Rhine and Maas sediments (Englert, 2003). According to Döring (1997) and Tillmann et al. (2008) the uppermost aquifer can be broadly divided into three layers (Fig. 2a): A bottom layer composed of sandy to gravely grain size, which extends from 6 to 11.5 m depth and is characterized by varying sand to gravel ratio; a well sorted sand layer extending from 4 to 6 m depth; and a poorly sorted gravel layer extending from 1 to 4 m depth. The base of the aquifer is formed by thin layers of clay and sand, at approximately 12 m depth. On top of the aquifer, a loamy soil layer has developed. The groundwater level shows seasonal variations from 1 to 3 m depth. The aquifer sediments are characterized by an average clay content of 2%

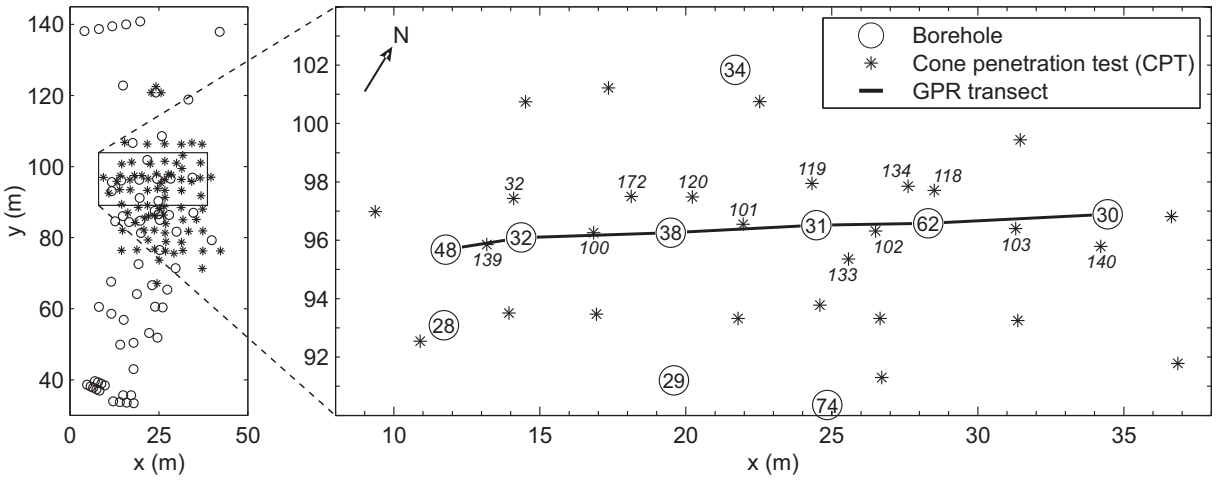

Fig. 1. Map of the Krauthausen test site with the location of boreholes (open circles) and cone penetration tests (asterixes). The black solid line in the close-up (right) shows the location of five adjacent cross-borehole GPR planes acquired in the central part of the test site. Selected cone penetration tests located close to the GPR transect are labeled with italic numbers.

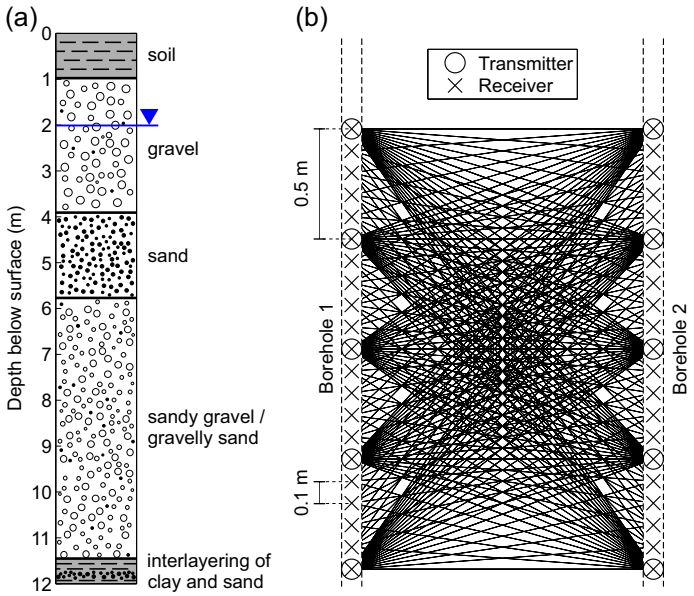

Fig. 2. (a) Generalized cross-section of the uppermost aquifer after Döring (1997) and Tillmann et al. (2008). (b) Schematic sketch of the crosshole GPR acquisition setup used in the present study. For clarity, the setup is shown for a vertical extension of 2 m only.

(Döring, 1997) and by a mean total porosity of 26% (Vereecken et al., 2000). The mean hydraulic conductivity based on the results of a large scale pumping test is $3.8 \cdot 10^{-3}$ m/s (Englert, 2003).

It is important to note that the generalized aquifer cross-section shown in Fig. 2a represents a simplified conceptual model. Treating the aquifer as a perfectly stratified medium is an oversimplification of the aquifer's true structure (at Krauthausen and elsewhere). For the true aquifer architecture we expect significant lateral variations in layer thickness and properties, as well as the existence of discrete non-layered structures. Characterization thereof is what the present study focuses on.

2.2. Crosshole ground penetrating radar tomography

2.2.1. Data acquisition

GPR data were acquired along a transect in the central part of the test site, where six closely spaced boreholes were available (Fig. 1). In total, the transect covers a lateral distance of 22.7 m and consists of five adjacent crosshole tomographic planes with individual borehole separations ranging from 2.6 to 6.2 m. We used the Sensors and Software pulseEKKO Pro system with 200 MHz antennas and a semi-reciprocal acquisition setup, with transmitter and receiver spacing of 0.5 m and 0.1 m, respectively (Fig. 2b). This setup was recently found to represent a compromise between sufficient ray coverage for high resolution inversion results, on the one hand, and affordable acquisition time and computational costs, on the other hand (Klotzsche et al., 2010; Oberröhrmann et al., 2013). In order to avoid refracted/reflected radar waves associated to the groundwater table (Klotzsche et al., 2010, 2012), GPR data were acquired only within the saturated zone. Measurements were conducted from 3 m depth, which was around 1 m below the groundwater table during the measurements, down to approximately 8–10 m depth, depending on the depth of the boreholes. Note that the transmitter and receiver positions within the

boreholes were accurately determined by using a logging tool that measures the lateral deviation of a borehole from a straight vertical line. This was necessary to avoid inversion artifacts.

2.2.2. Full-waveform inversion methodology

To infer the subsurface relative dielectric permittivity (ε) and electrical conductivity (σ) from the measured GPR data, we applied a full-waveform inversion. We used an inversion scheme introduced by Ernst et al. (2007a,b) and further developed by Meles et al. (2010) and Klotzsche et al. (2010). Here, we describe only briefly the major steps in the inversion scheme. For a more detailed description of the inversion procedure and its implementation, the reader is referred to Meles et al. (2010) and Klotzsche et al. (2010).

The overall goal of the inversion is to find the spatial distributions of ε and σ whose simulated radar response best matches the observed radar data. This is achieved in an iterative approach using a gradient method to minimize the misfit function

$$C = ||E^{mod} - E^{obs}||^2 \quad (1)$$

where E^{obs} is the observed radar data, for all transmitter-receiver combinations over the total observation time window, and E^{mod} is the corresponding data predicted by a forward model. Eq. (1) is a sample-by-sample comparison in which all data points are weighted equally. In order to enable the use of the forward model, which is based on a 2D finite difference time domain solution of Maxwell's equations, the observed data was converted from 3D to 2D using the approach by Bleistein (1986). Initial estimates for the distributions of ε and σ were derived using standard ray-based travel time and amplitude inversion (Holliger et al., 2001; Maurer and Musil, 2004). The full-waveform inversion was performed with the ray-based inversion results as starting models and with an effective source wavelet obtained through a deconvolution method (Ernst et al., 2007b). For each iteration of the full-waveform inversion, the wavefield predicted by the forward model is subtracted from the observed wavefield to calculate the residual wavefield. Local gradients for the ε and σ models are computed through a cross correlation of the back-propagated residual wavefield and the model-predicted wavefield. The gradient indicates if the model parameter values should be increased or decreased in order to reduce the misfit function. In addition, individual step lengths for ε and σ are determined which indicate the magnitude of the model updates. The ε and σ models are then simultaneously updated using the derived gradients and step lengths (Meles et al., 2010). Except from a smoothing of the gradient, no regularization is applied. Note that in order to avoid inversion artifacts close to the boreholes, model updates are suppressed within the domain closer than 30 cm to the boreholes. The updated ε and σ models are used to parametrize the forward model in the subsequent iteration step until the iteration is stopped when the root mean squared (RMS) misfit between model-predicted and observed data changes less than 1%.

It should be noted that the full-waveform inversion critically depends on adequate starting models for the ε and σ distribution. More precisely, for each transmitter-receiver combination, the observed data and the model-predicted data (obtained initially with the starting models) need to show an overlap within half the dominant wavelength in order to ensure proper convergence of the full-waveform inversion. If the offset between observed and modeled data is greater than half the dominant wavelength, the full-waveform inversion will converge to a local minimum and give unreliable results (Meles et al., 2011; Klotzsche et al., 2014). To ensure proper convergence of the full-waveform inversion, we carefully checked the match between observed and initially model-predicted data, prior to running the full-waveform inversion.

Another important step in the full-waveform inversion is the definition of perturbation factors for ε and σ, which are required for the computation of the model update step lengths (Meles et al., 2010). We determined appropriate values for the perturbation factors by testing the convergence of the full-waveform inversion with a range of values prescribed for the perturbation factors. With appropriate perturbation factors, the full-waveform inversion converges smoothly toward the optimal solution (maximal reduction of the RMS misfit), whereas too high or too low perturbation factors can be identified by non-smooth convergence and/or minor reduction of the RMS misfit. Note that the full-waveform inversion typically converges to the optimal solution for quite a range of perturbation factors (i.e. within that range the inversion results are robust with regard to changes in perturbation factors), which makes it relatively easy to find appropriate values for the perturbation factors, in practice.

2.3. Complex Refractive Index Model (CRIM)

Petrophysical relationships can be used to translate electrical properties obtained from GPR into hydrogeologically more relevant properties such as soil moisture or porosity. Several empirical, semi-empirical and theoretical relationships have been proposed in the literature (Topp et al., 1980; Dobson et al., 1985; Linde et al., 2006; Brovelli and Cassiani, 2008; Steelman and Endres, 2011). Commonly used approaches are so called mixing models, which are based on the intuitive idea that the bulk permittivity of a multi-phase medium can be related to the permittivities of the individual phases. In its general form, the mixing formula for an n-phase medium is

$$\varepsilon_b^\alpha = \sum_{i=1}^{n} V_i \varepsilon_i^\alpha \quad (2)$$

where ε_b is the bulk permittivity of the medium, V_i and ε_i are the volume fraction and the permittivity of the i-th phase, and α describes the geometrical arrangement of the individual phases within the medium. For fully saturated porous media, Eq. (2) can be written as

$$\varepsilon_b^\alpha = (1-\phi)\varepsilon_s^\alpha + \phi\varepsilon_f^\alpha \quad (3)$$

where φ is the porosity, and ε_s and ε_f are the permittivities of the solid grain matrix and of the pore fluid, respectively. The exponent α has theoretical upper and lower boundaries of 1 and -1, corresponding to the cases where individual phases are arranged in layers parallel and perpendicular to the applied electric field, respectively (Brown, 1956). Birchak et al. (1974) argued that for an isotropic phase arrangement, α should take a value of 0.5, which is equivalent to a volumetric average of the complex index of refraction. With $\alpha = 0.5$, Eq. (2) becomes the Complex Refractive Index Model (CRIM) (Birchak et al., 1974). Although the CRIM relationship is based on an oversimplified description of the complexity of natural porous media (Dobson et al., 1985; Brovelli and Cassiani, 2008), the CRIM has generally been found to agree well with experimental data and to produce adequate results for various types of soils (Roth et al., 1990; Robinson et al., 2003). In the present study, we apply the CRIM to convert bulk permittivity, obtained from GPR full-waveform inversion, into porosity, by rearranging Eq. (3) to

$$\phi = \frac{\sqrt{\varepsilon_b} - \sqrt{\varepsilon_s}}{\sqrt{\varepsilon_f} - \sqrt{\varepsilon_s}} \quad (4)$$

2.4. Cone penetration tests

A total number of 78 cone penetration tests (CPT) were conducted at Krauthausen and are described in detail by Tillmann

et al. (2008). The CPT survey focused on the central area of the site, where CPT were performed with a horizontal sampling interval of around 1–3 m (Fig. 1). At each CPT location, vertical profiles of mechanic cone resistance, natural gamma, bulk density and water content were obtained down to an average depth of approximately 13 m, covering the entire thickness of the uppermost aquifer. For a limited number of CPT, additional measurements of electrical conductivity and pore water pressure were conducted. Note that the sleeve friction, a commonly measured CPT parameter, was not measured in this study. The vertical sampling interval for all measurements was 10 cm. In the present study, we focus on a subset of 13 CPT, which were selected due to their close proximity to the GPR transect. The exact locations and ID numbers of the selected CPT are shown in Fig. 1.

2.5. Hydraulic conductivity from flowmeter test and grain size

Flowmeter tests at the Krauthausen site were conducted by Schneider (1995) and are described by Li et al. (2008). In the field, a constant pumping rate of $Q_p = 1500$ l/h was applied for a sufficiently long time to establish pseudo steady state conditions in the vicinity of the borehole. An electromagnetic flowmeter was used to measure the cumulative vertical flow rate in the borehole as function of depth. Measurements were conducted every 10 cm, starting at the deepest and ending at the highest accessible point within the filtered length of the borehole. If flow toward the borehole is assumed horizontal and there is no ambient flow in the borehole, then the increase of the cumulative flow rate at increment i, ΔQ_i, can be used to calculate the hydraulic conductivity (Javandel and Witherspoon, 1969; Molz et al., 1989).

$$K_i = \frac{\Delta Q_i b}{Q_p \Delta z_i} \overline{K} \tag{5}$$

where K_i is the horizontal hydraulic conductivity in the aquifer at increment i, b is the aquifer thickness, Δz_i is the thickness of the ith measurement increment, and $\overline{K}$ is the aquifer's depth averaged hydraulic conductivity. Note that we applied Eq. (5) with a constant increment of $\Delta z_i = 20$ cm and with $\overline{K}$ obtained from a large scale pumping test conducted in the central part of the test site (Englert, 2003).

In addition, hydraulic conductivity was estimated from grain size. For a limited number of boreholes at Krauthausen, sediment samples were extracted during drilling and the grain size distribution was determined through sieve analysis (Vereecken et al., 2000). The grain size data were used to derive hydraulic conductivity estimates based on the empirical relationship given by Bialas and Kleczkowski (1970)

$$K = 0.0036 d_{20}^{2.3} \tag{6}$$

where K is the hydraulic conductivity and d_{20} is the 20th percentile of the sediment particle size. According to Bialas and Kleczkowski (1970), Eq. (6) applies for sediments with a coefficient of uniformity, U, in the range of $0.2 < U < 60$, in which U is defined as the ratio of the 60th and 10th percentile of the particle size. It should be noted that the indirect method of estimating hydraulic conductivity based on grain size can be generally expected to be less reliable compared to methods that directly measure flow properties (such as pumping tests or flowmeter tests) because hydraulic conductivity is related to the pore structure rather than simply to the grain size (Koltermann and Gorelick, 1996).

In the present study we apply Eqs. (5) and (6) to obtain hydraulic conductivity profiles for borehole B32, which is one of the boreholes within the GPR transect (Fig. 1).

2.6. Cluster analysis

The principle of cluster analysis is to partition multivariate data into relatively homogeneous units by grouping data points based on their distances in a multi-dimensional parameter space. Data pre-processing typically involves data normalization (z-score) to assign similar weights to each measured variable and principal component analysis to reduce data dimensions which facilitates cluster analysis and data visualization. Many different clustering approaches exist (Everitt et al., 2001; MacKay, 2002). Generally, one can distinguish between hierarchical methods that produce nested clusters (i.e. clusters are embedded in others) and partitioning methods that produce a unitary classification into a pre-defined number of clusters. While partitioning techniques are known to be computationally more efficient than hierarchical methods, they require additional user-made specifications such as the number of clusters or the initial cluster centroid positions (Everitt et al., 2001).

Moreover, a distinction can be made between crisp and fuzzy clustering techniques. Crisp methods assign each data point to only exactly one cluster (i.e. to the most likely one), whereas fuzzy methods assign each data point a partial membership to all clusters (e.g. Paasche et al., 2010). A commonly applied crisp partitioning method is the k-means approach (MacQueen, 1967). The k-means algorithm partitions data points into a pre-defined number of clusters by minimizing the sum of distances from each data point to its cluster centroid over all clusters. Due to its conceptual simplicity and its computational efficiency, the k-means algorithm allows rapid classification of large multivariate data sets in a straight-forward manner. A notable limitation of k-means clustering is that all clusters are assumed to have the same isotropic variability (i.e. clusters are assumed to be spherical and of same size). This can cause problems when applied to data characterized by clusters with non-spherical shape and/or different size (MacKay, 2002; Rogiers, 2013). For the interpretation of such data sets, more flexible clustering techniques such as model-based clustering (Doetsch et al., 2010; Rogiers, 2013) or density-based clustering (Ester et al., 1996) can be favorable. Despite its limitations, however, the k-means algorithm has been proven useful to extract the basic structural information from various types of multivariate data including airborne geophysical data (Anderson-Mayes, 2002), grain size data (Riva et al., 2006) and tomographic geophysical data (Dietrich et al., 1998; Tronicke et al., 2004; Dietrich and Tronicke, 2009).

In the present study, we applied the k-means algorithm to partition the bivariate GPR inversion results (permittivity and electrical conductivity) into clusters. Prior to the cluster analysis, permittivity and electrical conductivity were z-transformed to assign similar weights to the two parameters. A critical step in the cluster analysis is the specification of the number of clusters. To determine the number of natural clusters in a data set, we employed the variance ratio criterion (VRC) (Calinski and Harabasz, 1974; Tronicke et al., 2004; Dietrich and Tronicke, 2009). Application of the VRC involves running the cluster analysis with different values prescribed for the number of clusters and calculating

$$\mathrm{VRC} = \left[\frac{SS_B}{(k-1)}\right] \Big/ \left[\frac{SS_W}{(n-k)}\right] \tag{7}$$

where SS_B is the between cluster sum-of-squares, SS_W is the within clusters sum-of-squares, k is the number of clusters and n is the number of samples. The number of clusters that maximizes the VRC value is supposed to optimally represent the data (Calinski and Harabasz, 1974). Because the final partition can be sensitive

to the randomly selected initial cluster distribution, the code was run multiple times to ensure stability of the final solution.

In a similar manner, we applied the *k*-means algorithm to the multivariate data from 13 CPT profiles located close to the GPR transect (Fig. 1). As described in Section 2.4, vertical profiles of cone resistance, gamma ray, bulk density and water content were measured at each CPT location, whereas electrical conductivity and pore water pressure were measured only at some CPT locations. To avoid dealing with incomplete data, we conducted the cluster analysis by considering only the measurements available for all CPT (i.e. cone resistance, gamma ray, bulk density, water content). Prior to the cluster analysis, the CPT data were z-transformed and converted into principal components. The first three principal components were used for the cluster analysis, while the fourth principal component was dropped because it explained only 5% of the total variance. The number of clusters was assigned according to the variance ratio criterion.

3. Results and discussion

3.1. GPR full-waveform inversion results and comparison with CPT data

A full-waveform inversion was applied to infer the subsurface permittivity and electrical conductivity along the transect shown in Fig. 1. The obtained tomographic images are shown in Figs. 3a and 4a, respectively. Black circles and crosses show the exact transmitter and receiver positions within the boreholes, determined by deviation log. Shaded areas depict regions outside of the tomographic cross-section. It is important to note that each of the five cross-borehole planes was inverted separately, i.e. independent from the adjacent planes. Nevertheless, consistent structures in the permittivity and electrical conductivity distribution can be observed left and right of the boreholes, which indicates robust inversion results. Convergence of the full-waveform inversion for the individual crosshole planes was reached after 16 iterations minimum (B62-B30) and 27 iterations maximum (B31-B62). Compared with the ray-based inversion results, the full-waveform inversion led to a reduction in RMS misfit of 51% minimum (B48-32) and 62% maximum (B32-B38). The stability of the final solution was controlled by running the full-waveform inversion repeatedly with different values prescribed for the perturbation factors (not shown here). Because we found the inversion results to be robust over quite a wide range of perturbation factors, we can expect that the obtained results are reliable.

The tomographic images obtained through full-waveform inversion show a high level of detail and contain spatial structures at the decimeter scale (Figs. 3a and 4a). Note that similar to the findings of Klotzsche et al. (2013, 2014) the full-waveform inversion considerably improved the spatial resolution of the initially derived ray-based inversion results (not shown here). A striking feature in the GPR images is the strong increase in both the permittivity and the electrical conductivity between 3 and 4 m depth which indicates a distinct sedimentologic boundary in the aquifer material at that depth. To validate the reliability of the obtained GPR results, we compared them with cone penetration test data.

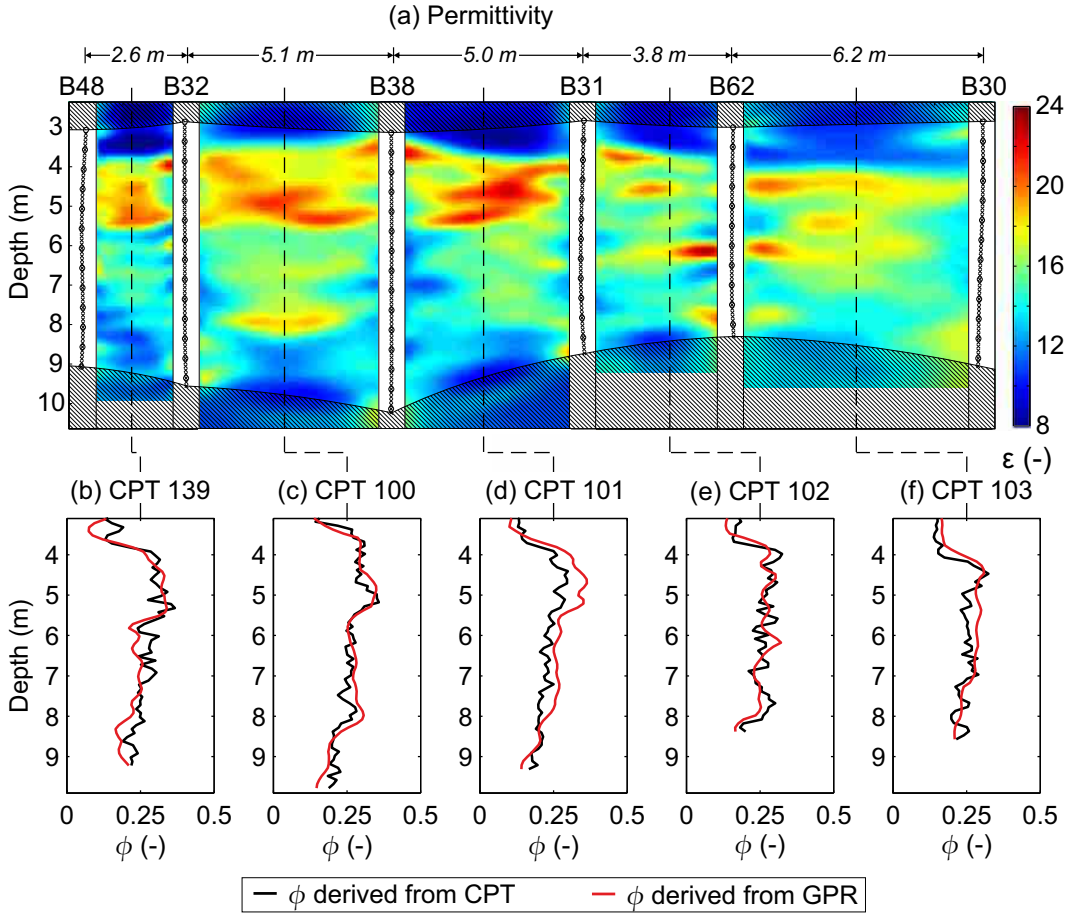

Fig. 3. (a) Permittivity full-waveform inversion results along the GPR transect. (b–f) Comparison of vertical porosity profiles derived from CPT (neutron logs) with co-located GPR permittivities converted into porosity using the CRIM (Eq. (4)). The exact locations of the CPT profiles within the GPR transect are indicated by the dashed lines.

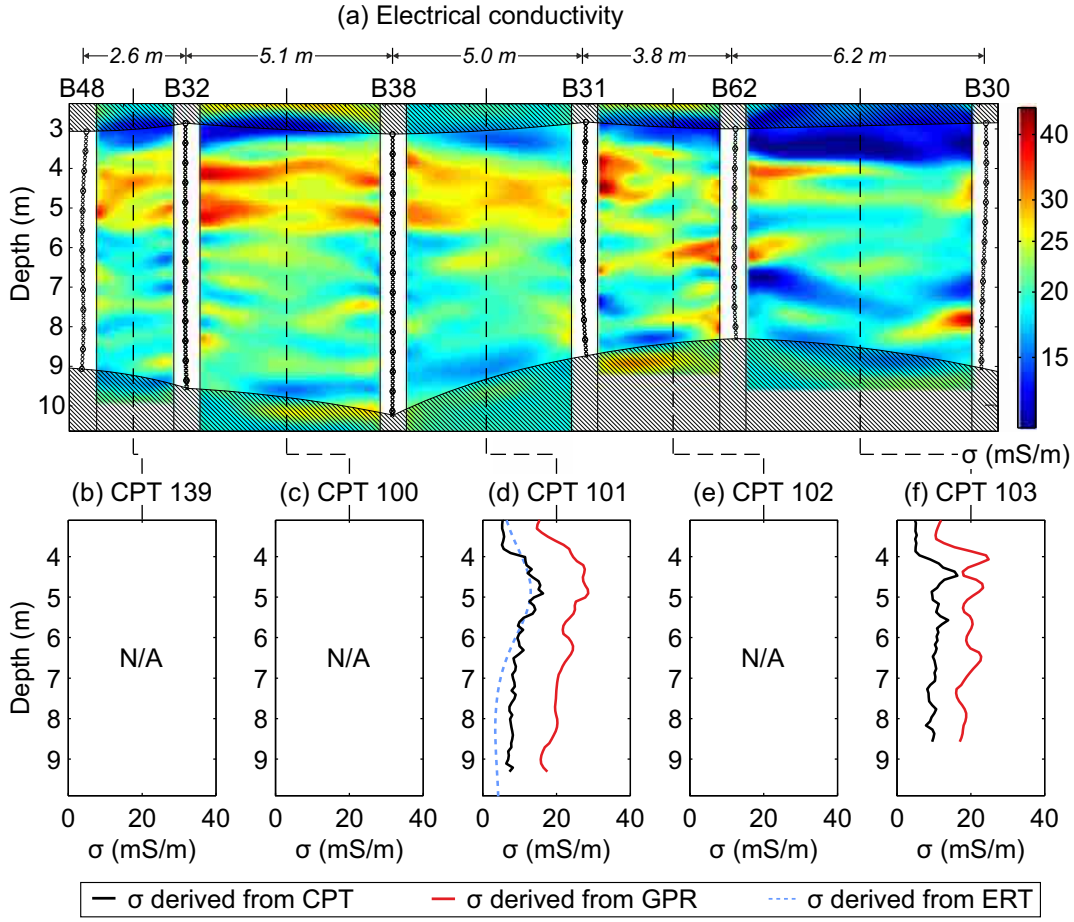

Fig. 4. (a) Electrical conductivity full-waveform inversion results along the GPR transect. (b–f) Comparison of vertical profiles of electrical conductivity derived from CPT and GPR. Due to technical problems during the CPT measurements, electrical conductivity logs are available only for CPT 101 and 103. Along CPT 101, the GPR and CPT results can additionally be compared with ERT results (Müller et al., 2010).

As can be seen in Fig. 1, five CPT are located directly within the GPR transect, and thus, can be compared with the GPR results. In the following, we show a comparison of porosity estimates derived from GPR and from CPT; and a comparison of electrical conductivity estimates derived from GPR and from CPT.

3.1.1. Derivation of porosity from GPR and CPT

GPR porosities were derived by converting permittivity inversion results into porosities using the CRIM relation (Eq. (4)). The CRIM was parametrized with $\varepsilon_f = 84$, which represents the permittivity of water at 10 °C (Eisenberg and Kauzmann, 1969), and with $\varepsilon_s = 4.5$, which represents the solid grain permittivity of quartz (Carmichael, 1982). Note that the choice of using the permittivity of quartz for ε_s is based on the results of picnometer measurements, which gave a mean sediment density of 2.65 g/cm^3 at Krauthausen (Vereecken et al., 2000) which corresponds to the density of quartz.

CPT porosities were derived from neutron log data. Tillmann et al. (2008) used a calibration that was performed by Elgoscar 2000 Ltd. in Budapest, Hungary, to relate neutron log data to water content, which, under saturated conditions and in the absence of significant amount of clay, represents porosity. We critically reviewed the calibration used in Tillmann et al. (2008) by comparing porosity data derived from CPT with laboratory porosity measurements. The black solid line in Fig. 5a shows the porosity of sediment samples extracted from borehole B7, which is located in the northern part of the test site. The sediment samples were oven-dried and their porosity was determined by measuring their weight, volume and dry matrix density in the laboratory (Döring, 1997). The red dashed line shows porosities obtained by applying the calibration used in Tillmann et al. (2008) to neutron log data from a CPT located close to borehole B7. Obviously, the CPT porosities reproduce the trend of the laboratory measurements quite well, but they show consistently higher absolute values. The blue dashed line shows the effect of applying a simple constant-shift correction ($\varphi_{corrected} = \varphi - 0.08$) to the CPT porosities. Obviously, this leads to a much better match of the two curves.

Another indication that the calibration used by Tillmann et al. (2008) yields overestimated porosity values is shown in Fig. 5b. The cross-plot shows how CPT derived porosities compare with GPR porosities predicted by the CRIM. The calibration according to Tillmann et al. (2008) clearly results in distinctly higher porosities derived from CPT (crosses) compared with the CRIM-predicted porosities (black solid line). Corrected CPT porosities (filled circles), however, scatter closely around the CRIM, and thus agree fairly well with the porosity derived from GPR. Note that changing the value for ε_s in Eq. (4), would result in a shift of the CRIM curve along the *x*-axis in Fig. 5b. A satisfactory fit between the CRIM curve and the Tillmann et al. (2008) calibrated data could be obtained by using an ε_s-value of 1.8 instead of 4.5. This must be considered, however, to be an unrealistically low value for ε_s at Krauthausen, because it is known from previous studies that the aquifer material at Krauthausen basically consists of quartz (Döring, 1997; Vereecken et al., 2000) and the ε_s-value of quartz is 4.5 (Carmichael, 1982). We therefore assume that, for unknown reasons, the calibration used by Tillmann et al. (2008)

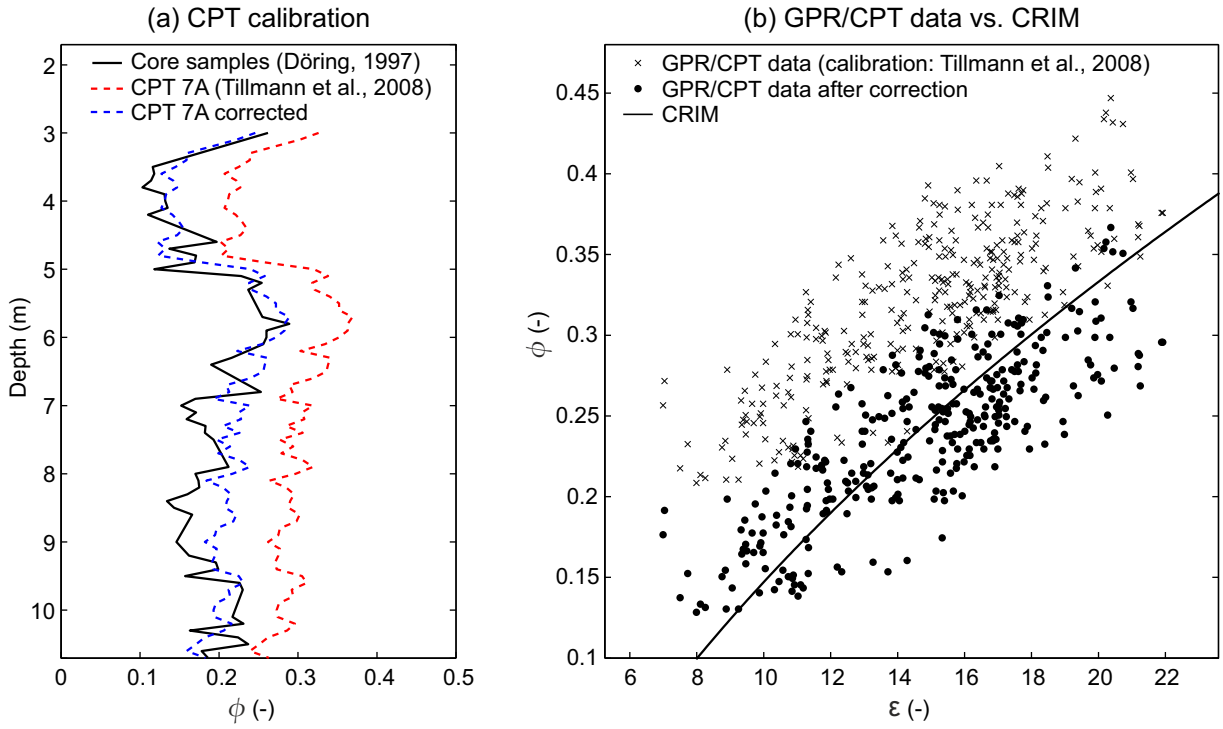

Fig. 5. (a) Comparison of CPT porosity estimates with laboratory porosity measurements. (b) Cross-plot of co-located GPR and CPT data. The *x*-axis denotes the permittivity derived from GPR. The *y*-axis denotes the porosity derived from CPT. Black solid line shows porosities predicted by the CRIM (Eq. (4)).

overestimated the true sediment porosity. A simple constant-shift correction ($\varphi_{corrected} = \varphi - 0.08$), however, seems to be applicable to compensate for the overestimation. In the remainder of this paper, thus, corrected CPT porosities are used.

3.1.2. Quantitative comparison of GPR and CPT results

Figs. 3b–f and 4d and f show porosity and electrical conductivity profiles derived from GPR and CPT. While the GPR and CPT porosity profiles match quite well, notable deviations exist between the GPR and CPT electrical conductivity profiles. To assess the agreement between GPR and CPT results in a quantitative manner, we calculated correlation coefficients and linear regression parameters. While the correlation coefficient measures how close the observed values come to falling on a straight line in a cross-plot, the slope and intercept of the linear regression allow to assess the deviations from a 1:1 relationship (e.g. Isaaks and Srivastava, 1990). Results for the porosity and for the electrical conductivity data are shown in Fig. 6a and b, respectively.

Porosities derived from GPR and CPT show a strong linear relationship with a linear correlation coefficient of $r = 0.8$. Moreover, the slope and intercept of the linear regression are close to 1 and 0, respectively, which means that the data fall close to the 1:1 line.

The picture is different for the electrical conductivity. First, the correlation between GPR and CPT results is less pronounced ($r = 0.67$). More importantly, while the slope of the linear regression is close to 1, the intercept significantly departs from 0. In other words, the GPR and CPT electrical conductivity profiles agree fairly well regarding the variations in conductivity, but they show a static shift in absolute values. To further investigate the discrepancy in absolute values, we compare the electrical conductivity obtained from GPR and CPT additionally with results from Müller et al. (2010) who investigated electrical conductivity at Krauthausen based on cross-borehole electrical resistivity tomography (ERT). At CPT location 101, co-located electrical conductivity values are available from CPT, GPR and ERT. The vertical profiles obtained from the three methods are compared in Fig. 4d. Obviously, the absolute electrical conductivity values derived from ERT better match the CPT results than the GPR results. Apart from that, it is interesting to note that the three methods show considerable differences in spatial resolution, i.e. ERT basically misses the small-scale variability which is most pronounced in the CPT profile and still clearly visible in the GPR profile.

In the following, we discuss two possible explanations why the absolute conductivity values derived from GPR are higher than the absolute values derived from CPT and ERT. One explanation is that the different absolute values are caused by the inherent differences of the applied methods: ERT and CPT infer electrical conductivity on the basis of direct current resistivity measurements, whereas GPR uses the attenuation of the GPR signal to infer the electrical conductivity at higher frequencies. The attenuation of a GPR signal in the subsurface can be affected by (frequency-dependent) attenuation effects caused by water relaxation or signal scattering (e.g. Davis and Annan, 1989). Because these effects cause an attenuation, which acts in addition to the attenuation caused by electrical conductivity, this could explain the higher absolute conductivities obtained from GPR.

Another possible explanation is that the higher absolute conductivity values derived from GPR are caused by biased starting models used in the full-waveform inversion. As described in Section 2.2.2, we derived starting models for the permittivity and conductivity by applying a ray-based travel time and amplitude inversion, prior to the full-waveform inversion. While ray-based methods generally provide reliable (but smooth) estimates for the permittivity, estimation of electrical conductivity is less straightforward and, in particular the absolute values of the electrical conductivity are typically less reliable (Holliger et al., 2001; Maurer and Musil, 2004). Unfortunately, inaccuracies in the absolute values of the electrical conductivity starting model are propagated into the amplitude of the estimated effective source wavelet used for the full-waveform inversion because wavelet and electrical conductivity model are coupled (Busch et al., 2012). As a

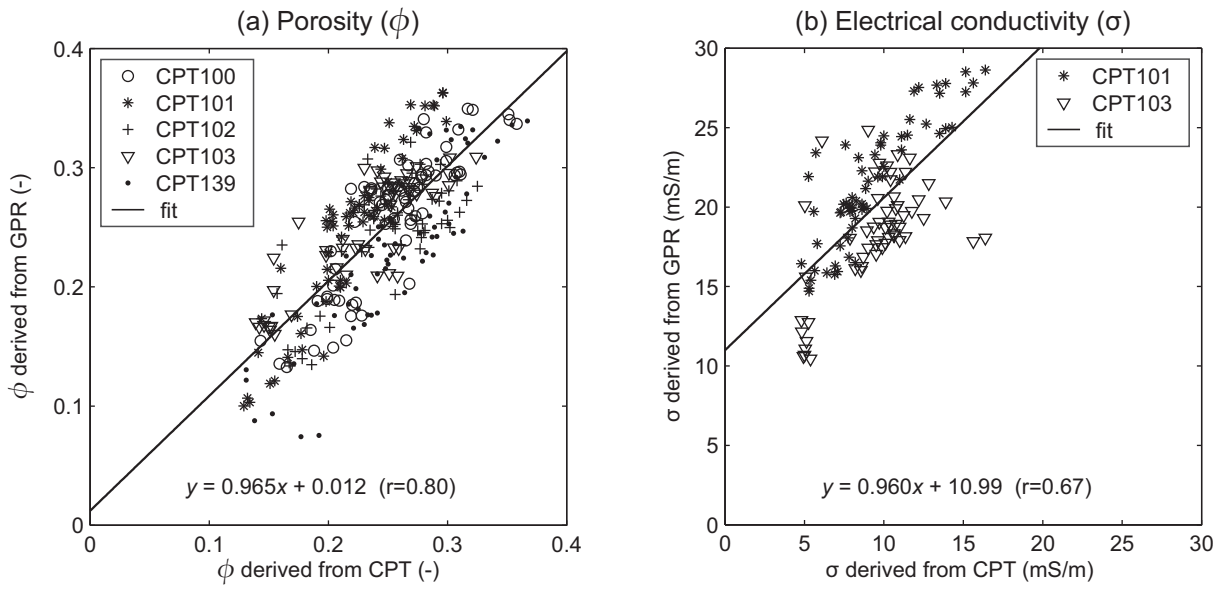

Fig. 6. (a) Cross-plot of porosities derived from CPT and GPR for the five profiles for which co-located porosity data exist (Fig. 3b–f). (b) Cross-plot of electrical conductivities derived from CPT and GPR for the two profiles for which co-located conductivity data exist (Fig. 4d and f). Regression lines through all data points are depicted in black. The corresponding straight-line equations are given at the bottom of the cross plot, *r* is the correlation coefficient.

consequence, absolute electrical conductivities obtained through full-waveform inversion would be biased if the absolute values of the electrical conductivity starting model were biased. As discussed in detail in Busch et al. (2012), a strategy to overcome this issue would be to update the wavelet simultaneously together with the conductivity and permittivity models during the full-waveform inversion.

Irrespective of the discrepancies in the absolute values, however, GPR and CPT results agree fairly well regarding the absolute spatial variations in electrical conductivity (slope of regression line is close to 1 (a = 0.96), and the correlation coefficient is 0.67). In the next section, we present the results of the cluster analysis. Because the cluster analysis interprets the differences in data rather than their absolute values, this allows us to exploit the electrical conductivity inversion results even if absolute values are uncertain.

3.2. Cluster analysis of GPR and CPT data

The cluster analysis was applied to classify the GPR and CPT data into clusters, related to sediment facies with different parameter signatures. Fig. 7a and b shows the clustered GPR and CPT data. Note that the cluster analysis was conducted independently with the GPR and the CPT data set. The number of clusters, prescribed in accordance to the variance ratio criterion, is three for the GPR data (Fig. 7c) and six for the CPT data (Fig. 7d). However, in the part of the aquifer cross-section where GPR and CPT data overlap, a consistent number of three clusters appear in both data sets and their spatial distribution in the aquifer cross-section shows a good match (Fig. 8b). As a measure for the consistency between the spatial distribution of GPR and CPT clusters, we calculated for each CPT profile the percentage of pixels for which the same cluster ID number was obtained from GPR and from CPT. The results are listed in Table 1. It is important to note that only five of the 13 CPT profiles are located directly within the GPR transect. The other eight CPT are located in a lateral distance of 1–1.5 m away from the GPR transect, which can be expected to lead to differences between CPT and GPR results. As can be seen in Table 1, the average agreement between CPT and GPR cluster assignment is indeed larger for the five CPT located close to the GPR transect (77%), than for the CPT located farther away from the transect (63%). Overall, the close agreement of the spatial distribution of GPR and CPT clusters suggests that the cluster analysis, although performed independently with GPR and CPT data, yet defined the same facies in the aquifer. This is a promising result because it suggests that the facies obtained from GPR provide a meaningful classification of the subsurface, not only with regard to electrical properties but also with regard to further sediment properties, such as those measured by CPT.

3.2.1. Reliability of the facies classification obtained through cluster analysis

Despite the overall consistency of the spatial distribution of GPR and CPT clusters, there are some locations in the aquifer cross-section where the cluster assignment based on GPR and CPT is inconsistent. This indicates an uncertainty of the facies classification at these locations. Fig. 9 shows the facies classification of co-located GPR and CPT data in a cross-plot of permittivity and electrical conductivity derived from GPR. Only the data along the five CPT profiles which are located directly within the GPR transect are used. For clarity the same color scale was used to represent GPR clusters and CPT clusters. This means, data points that were assigned the same cluster ID number based on GPR and based on CPT, have uniform color; data points for which the cluster assignment based on GPR and CPT is inconsistent, are two-colored. The legend in Fig. 9 lists all possible events, sorted by their number of occurrences (n). In total, there are 244 (i.e. 77%) consistent data points, and 74 (i.e. 23%) inconsistent data points. Interestingly, the inconsistent data points are not evenly distributed in the cross-plot. Only few inconsistent data points plot in the lower left corner and in the upper right corner, the majority of inconsistent data points are scattered around the borders between clusters. This suggests that there are regions in the permittivity–conductivity parameter space, where GPR and CPT facies assignment are more reliable; and there are other regions where GPR and CPT facies assignment are less reliable. Since the classification of facies based on GPR data was completely independent from the classification based on CPT data, inconsistencies in classification can be considered to be related to uncertainty of classification. We used the match/

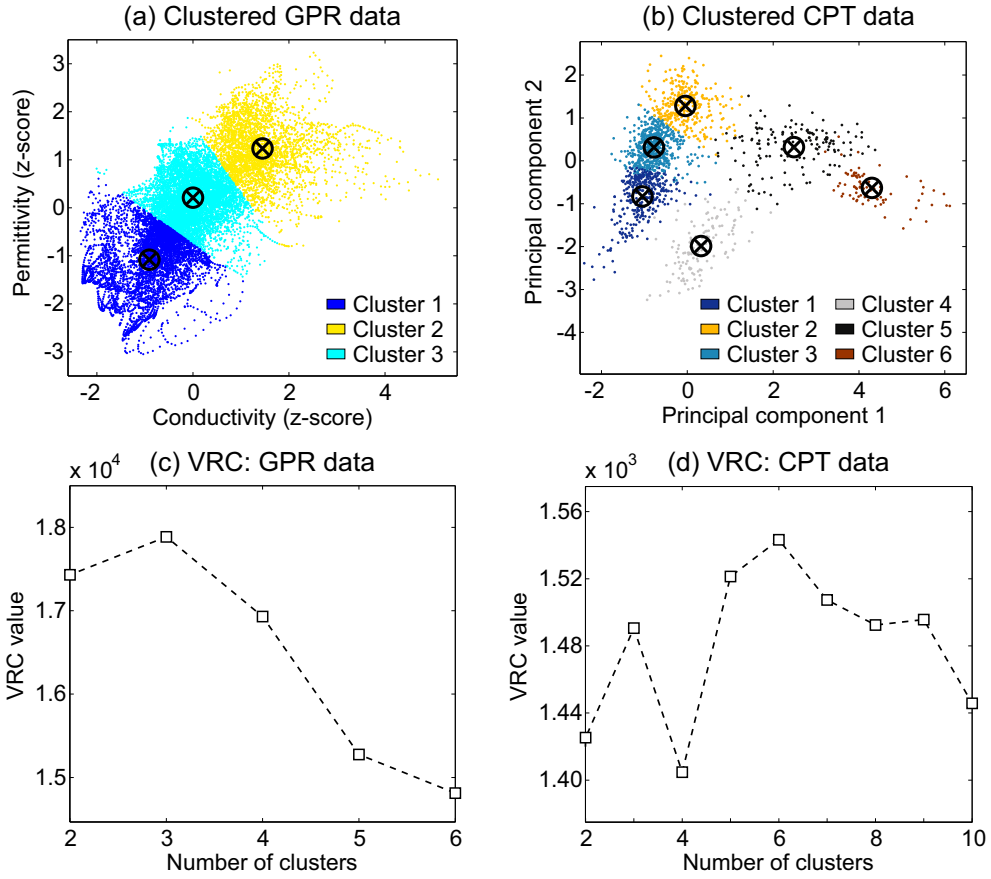

Fig. 7. (a and b) *k*-means clustering of GPR and CPT data. (c and d) The optimal number of clusters according to the variance ratio criterion (Eq. (7)).

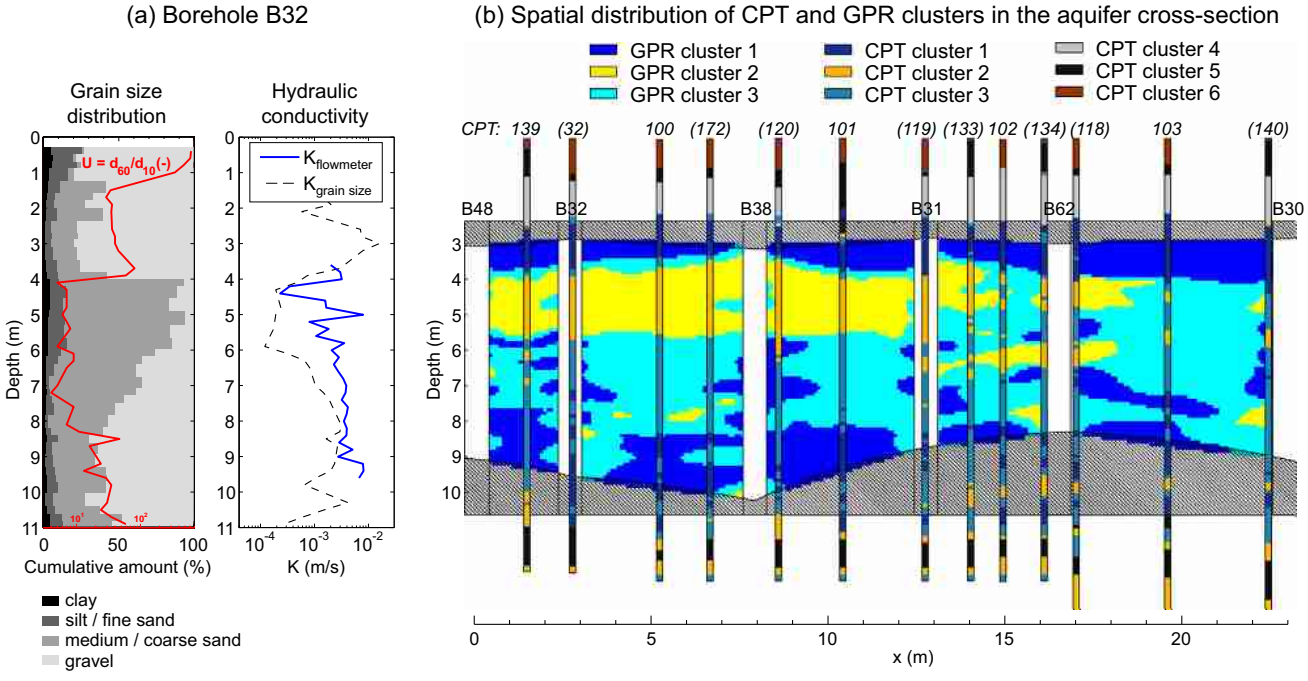

Fig. 8. (a) Grain size distribution and hydraulic conductivity for borehole B32 (second borehole from left in the GPR transect). Red line represents the coefficient of uniformity, *U*. Blue and dashed black line represent hydraulic conductivity, *K*, derived from flowmeter test and from grain size, respectively. (b) Spatial distribution of GPR and CPT clusters. Parentheses indicate CPT that are not located directly within the GPR transect but at a certain lateral distance from it. Exact lateral displacements for the CPT are listed in Table 1. (For interpretation of the references to colour in this figure legend, the reader is referred to the web version of this article.)

Table 1
Consistency of GPR and CPT cluster assignment along CPT profiles.

CPT	Distance to GPR transect (m)	Consistent classification*	
		Single profile (%)	Averaged (%)
139	0.1	55	
100	0.1	89	
101	0.2	91	77
102	0.2	74	
103	0.3	73	
32	1.3	–	
172	1.2	89	
120	1.2	57	
119	1.5	–	63
133	1.2	64	
134	1.3	56	
118	1.1	67	
140	1.1	42	

* GPR cluster ID number = CPT cluster ID number.

mismatch between the GPR and CPT facies assignment at co-located locations as a basis to approximate the reliability of the facies classification in the entire GPR transect. We defined the ratio R for a certain parameter vector $\vec{X}$ in the GPR derived permittivity–conductivity parameter space as:

$$R(\vec{X}) = \frac{\frac{1}{n}\sum_{i=1}^{n}(\vec{X}-\vec{P}_i)^2}{\frac{1}{m}\sum_{j=1}^{m}(\vec{X}-\vec{Q}_j)^2} \quad (8)$$

where $\vec{P}_{1,\ldots,n}$ and $\vec{Q}_{1,\ldots,m}$ represent the parameter vectors of consistently and inconsistently assigned data points for the respective cluster. For example, if $\vec{X}$ was assigned to cluster 1, then $\vec{P}$ would represent the data points that were consistently assigned to cluster 1 based on GPR and CPT; and $\vec{Q}$ would represent the data points that were assigned to cluster 1 only either by GPR or by CPT. Low values for R indicate high reliability of the facies classification because $\vec{X}$ has a permittivity–conductivity signature similar to those data points where GPR and CPT cluster assignment are consistent; high values for R indicate low reliability of the facies classification because $\vec{X}$ has a permittivity–conductivity signature similar to those data points where GPR and CPT cluster assignment are inconsistent. Note that R does not represent the reliability of the GPR or CPT data themselves. R solely approximates the reliability of the cluster analysis based classification of the data into facies.

Fig. 10 shows the distribution of R values in the aquifer cross-section. The R value of a grid cell depends on its relative position, in the data space, to consistently and inconsistently classified data points. Sharp contrasts in R thus reflect the situation when spatially close cells differ in permittivity and/or conductivity and thus plot in data space regions with different densities of consistent/inconsistent points. As expected, high R values occur prevalently along the boundaries between facies (compare with Fig. 8b). This reflects our previous finding that the data points for which GPR and CPT cluster assignment are inconsistent generally plot close to the borders between clusters in the parameter space. It is interesting to note, however, that at some locations in the aquifer, facies boundaries are accompanied by only thin bands of high R values, while at other locations, facies boundaries are accompanied by considerably thicker bands of high R values. A thin band of high R values suggests little uncertainty of the exact location of the facies boundary; a thick band of high R values suggests larger uncertainty for the exact location of the facies boundary. We believe that these differences can be attributed to different types of sedimentologic boundaries within the aquifer. For instance, the uppermost facies boundary between 3 and 4 m depth is characterized by a considerably thin band of high R values (Fig. 10). At this depth, the grain size distribution in borehole B32 shows an abrupt change from gravel to underlying sand (Fig. 8a). This suggests that this boundary represents an

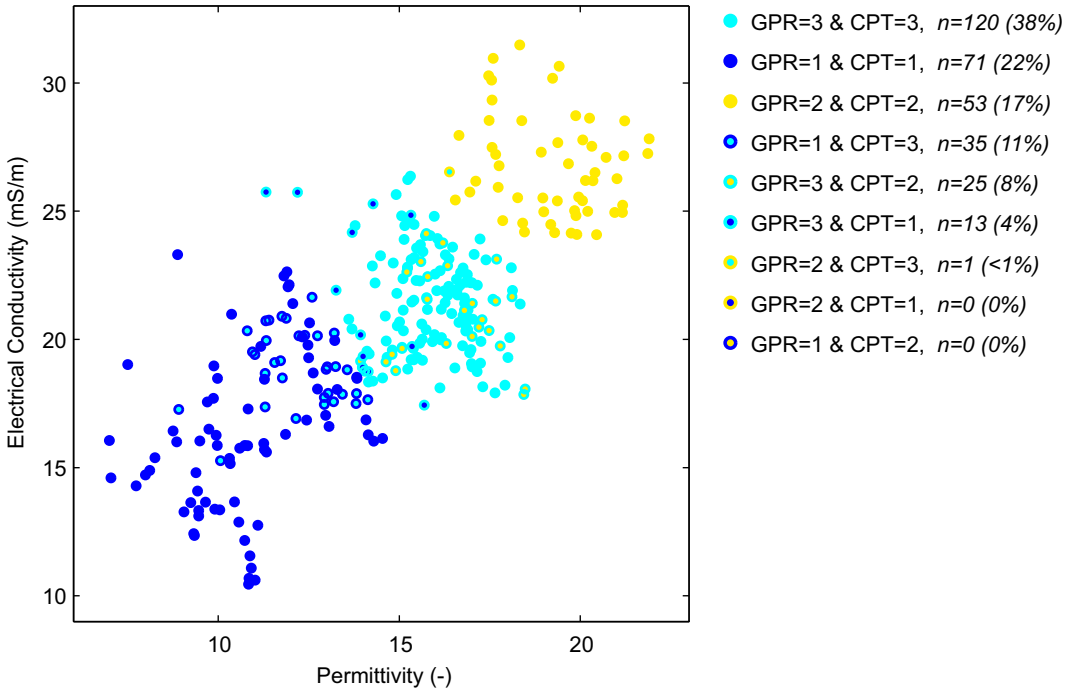

Fig. 9. Cluster assignment of co-located GPR and CPT data. Color of circle edges refer to the cluster assignment based on GPR. Color of circle inner area refer to the cluster assignment based on CPT. n is the number of occurrences. (For interpretation of the references to colour in this figure legend, the reader is referred to the web version of this article.)

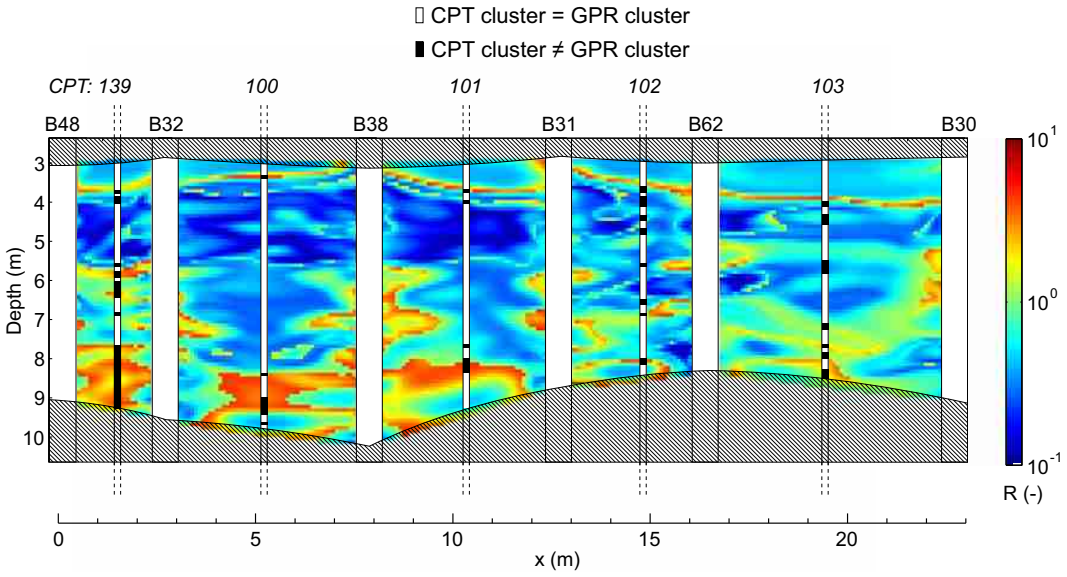

Fig. 10. Estimated reliability of the facies classification based on the match/mismatch between GPR and CPT cluster assignment at co-located locations (indicated in white/black). Low *R* values suggest high reliability, high *R* values suggest low reliability (see Eq. (8)).

erosional-surface boundary, where sedimentation was interrupted by a phase of erosion. At such a boundary, sediment properties can abruptly change and facies are clearly separated from each other. Note that a distinct boundary at that depth is also indicated by the full-waveform inversion results, which show an abrupt increase in permittivity and electrical conductivity between 3 and 4 m depth (Figs. 3a and 4a).

In contrast, in the lower part of the aquifer cross-section (7–10 m depth), facies boundaries are generally characterized by relatively thick bands of high *R* values (Fig. 10). At this depth, the grain size in B32 shows a gradual increase with increasing depth (Fig. 8a) and the permittivity and electrical conductivity distributions show relatively mild variations (Figs. 3a and 4a). Gradual changes in subsurface properties can be caused by gradual changes in deposition conditions or by cyclic deposition patterns, which are commonly observed in fluvial systems (Miall, 1996). If a sediment is characterized by gradual changes in properties, however, it is difficult to define facies and to delineate the boundaries between them.

This highlights an important implication of using crisp clustering methods (such as *k*-means) to define subsurface facies. Crisp cluster algorithms partition each data point to one of the clusters. More specifically, if a data point plots close to the border between two clusters in the parameter space, small changes in the parameter signature of this data point will result in the assignment of that point to either the one or the other cluster. In the presence of abrupt changes in the subsurface properties, this is not an issue because there are only few or no data points which lie between clusters in the parameter space. Such a boundary seems to exist between 3 and 4 m depth, where the thin band of high *R* values suggests that the exact location of the corresponding facies boundary is accurately defined. In contrast, if subsurface properties change gradually, more data points are characterized by a parameter signature, which plots close to the borders between clusters in the parameter space. In this case, data points cannot be assigned unambiguously to either the one or the other cluster and facies are not clearly separated from each other. This seems to be the reason for an increased uncertainty of the facies classification in the lower part of the aquifer where thick bands of high *R* values suggest a larger uncertainty of the exact location of facies boundaries.

In conclusion, our analysis suggests that the simple *k*-means approach used in the present study is an applicable tool to delineate facies boundaries if the subsurface is characterized by distinct sedimentologic changes. However, if the subsurface is characterized by rather subtle or gradual sedimentologic changes, the exact location of facies boundaries obtained from *k*-means clustering should be interpreted with caution because the crisp classification of data points that fall between clusters may be misleading. In such environments, fuzzy clustering approaches, which yield additional information about the quality and the internal consistency of the obtained data classification (e.g. Paasche et al., 2010, 2012) might be beneficial.

3.2.2. Hydrogeological facies interpretation

In this section, we discuss which type of sediment is related to the different clusters. We first briefly discuss CPT clusters 4–6, which occur in the unsaturated zone and in the deeper part of the aquifer where no co-located GPR data exist. Then we focus on GPR and CPT clusters 1–3, which occur in the central part of the aquifer cross-section where CPT and GPR data overlap.

At the top of each CPT profile, the CPT clusters 5 and 6 occur (Fig. 8b). Both clusters are characterized by large natural gamma values and by low cone resistance values (Fig. 11). This suggests a soft and clay-rich sediment. Note that CPT cluster 5 occurs again near the bottom of the profiles at approximately 11–12 m depth, where according to Tillmann et al. (2008) the clay layer at the bottom of the uppermost aquifer is located. We interpret CPT clusters 5 and 6 as clay-rich sediments which form the top soil layer and the lower boundary of the uppermost aquifer. The reason why they are not grouped together in just one cluster in the cluster analysis seem to be low bulk density and low water content values in the uppermost dry and less compacted soil decimeters.

In contrast to CPT cluster 5 and 6, the CPT cluster 4 shows large cone resistance values and small natural gamma values (Fig. 11). This suggests a hard material such as gravel or gravelly sand with only small amounts of clay. Note that CPT cluster 4 is separated from CPT cluster 1 by a near-horizontal boundary at approximately 2.3 m depth (Fig. 8b). The vertical position of that boundary corresponds to the groundwater level during the CPT survey (Tillmann et al., 2008). This indicates that the two clusters could represent the same type of material under saturated and under unsaturated conditions. The CPT data supports this interpretation, because the

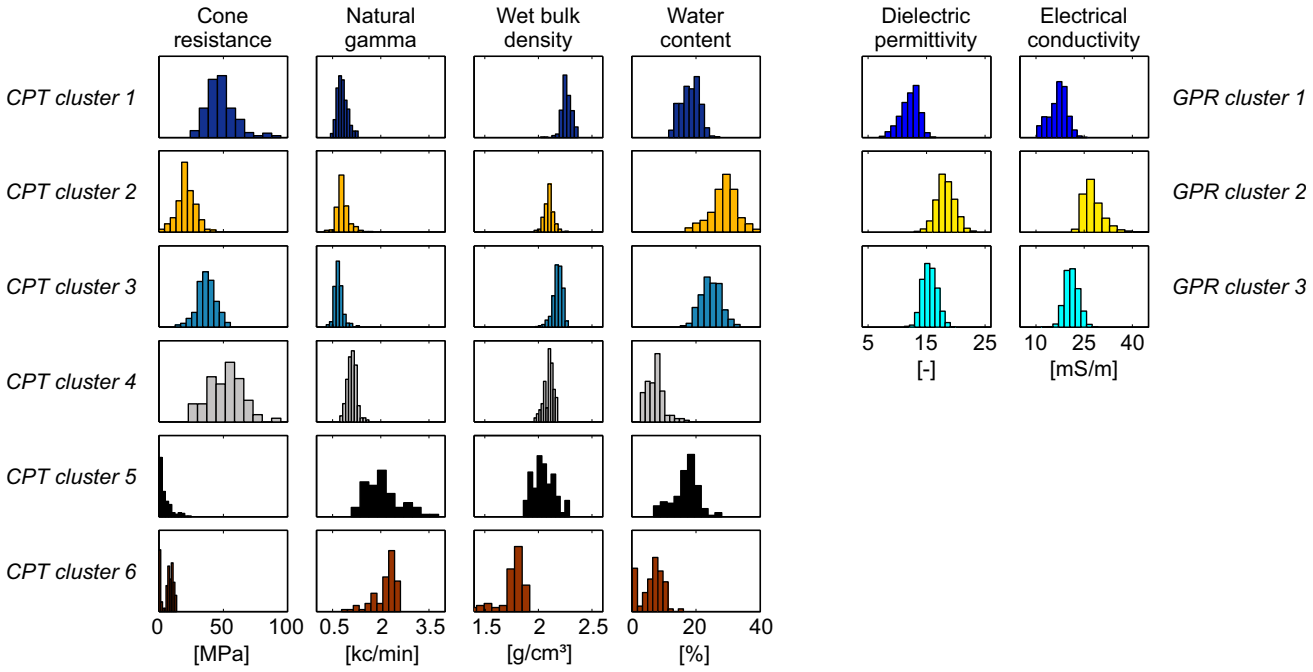

Fig. 11. Characteristic histograms for CPT clusters (left) and GPR clusters (right).

histograms of cone resistance and gamma activity derived for CPT clusters 1 and 4 look quite similar, while the histograms of water content and wet bulk density deviate for the two clusters (Fig. 11).

In the part of the aquifer cross-section where CPT and GPR data overlap, clusters 1–3 occur in both data sets. Comparison of the grain size distribution in borehole B32 (Fig. 8a) with the spatial distribution of GPR and CPT clusters close to this borehole shows that GPR and CPT cluster 1 occur in those depths where the grain size analysis shows gravel; GPR and CPT cluster 2 occur in those depths where the grain size analysis shows sand; and GPR and CPT cluster 3 occur where the grain size analysis shows an intermediate material such as a gravelly sand or a sandy gravel. This interpretation is supported by the histograms of cone resistance data, which show the largest values for CPT cluster 1, the smallest values for CPT cluster 2, and intermediate values for CPT cluster 3 (Fig. 11). The water content histograms, which under saturated conditions can be expected to represent porosity, suggest a relatively small porosity for CPT cluster 1, a relatively high porosity for CPT cluster 2 and an intermediate porosity for CPT cluster 3. As expected, the permittivity histograms for GPR clusters 1–3 show the same trend as the water content histograms for CPT clusters 1–3. Interestingly, also the electrical conductivity histograms show the same trend as the water content histograms. This suggests that the differences in electrical conductivity for GPR clusters 1–3 are mainly caused by differences in porosity. The reason for the correlation between porosity and electrical conductivity is probably that there are only minor changes in clay content in this part of the aquifer, which is supported by the fact that the histograms of gamma activity only slightly deviate for CPT clusters 1–3. With the clay content staying roughly constant, the electrical conductivity derived from GPR is mainly influenced by the electrical conductivity of groundwater, and thus, by changes in sediment porosity.

Note that the uniformity coefficient $U = d60/d10$ (red line in Fig. 8a) takes relatively high values in those depths where gravel occurs and relatively low values where sand occurs. This suggests that the higher porosity of the sand facies compared to the gravel facies can be explained by the better sorting of the sand facies compared to the gravel facies.

To evaluate if the facies derived from GPR and CPT provide a meaningful classification with regard to hydraulic conductivity, we compare the facies distribution with vertical profiles of hydraulic conductivity derived from a flowmeter test and from grain size data (Fig. 8a). Given the limited amount of hydraulic conductivity data, our goal is not to precisely determine quantitative hydraulic conductivity values for each facies but rather to evaluate if the derived facies show any correspondence to changes in hydraulic conductivity. It should be noted that, in principle, the (direct) flowmeter method can be expected to give more reliable results than the (indirect) grain size method. However, flowmeter results critically depend on proper well construction and well development and can be biased by ambient flow in the borehole (Molz et al., 1994).

Overall, flowmeter and grain size based hydraulic conductivity profiles agree relatively well in the lower part of the aquifer but depart from each other in the upper part of the profile. The grain size based hydraulic conductivity profile shows an obvious correlation with the spatial distribution of GPR and CPT clusters. The lowest values for the hydraulic conductivity are derived between 4 and 6 m depth, which match with the upper and lower boundary of GPR and CPT cluster 2, respectively. The highest values for the hydraulic conductivity are obtained at around 3 m depth where GPR and CPT cluster 1 occur. Intermediate hydraulic conductivity values are obtained from 6 to 9 m depth where GPR and CPT suggest alternating occurrence of clusters 1 and 3.

The flowmeter based hydraulic conductivity profile generally shows a comparable trend but it departs from the grain size based conductivity profile in the upper part of the aquifer. Changes in the flowmeter based hydraulic conductivities are not as clearly associated with the cluster boundaries as it is the case for the grain size based hydraulic conductivities. While the upper boundary of GPR and CPT cluster 2 (at 4 m depth) can be clearly recognized in the flowmeter based conductivity profile, the lower boundary at 6 m depth is only associated with a minor change in hydraulic conductivity. Moreover the profile between those boundaries (4–6 m depth) shows strong inhomogeneities. The distinct peak at 5 m depth represents a particularly high hydraulic conductivity value surrounded by low conductivity values. This suggests a significant

heterogeneity within cluster 2. It must be noted, however, that the peak consists of a single value only, and could represent a measurement error. The uppermost layer of GPR and CPT cluster 1 is, unfortunately, only partly covered by the flowmeter data because due to the technical setup, the flowmeter measurements could be conducted only below approximately 3.5 m depth. The hydraulic conductivity of cluster 1 in the uppermost layer can therefore not be evaluated based on the flowmeter data. It can be recognized, however, that the flowmeter based hydraulic conductivity profile shows relatively high values below 6 m depth, where GPR and CPT cluster 1 and 3 occur, and relatively low values between 4 and 6 m depth, where GPR and CPT cluster 2 occur (except for the one value peak at 5 m depth).

Putting all information together, the following interpretation can be derived: GPR and CPT cluster 1 show the distribution of a moderately-poorly sorted gravel facies, which occurs at the top of the GPR cross-section in one continuous layer, and close to the bottom of the GPR cross-section in several isolated patches. Based on the water content values of CPT cluster 1, the gravel facies is characterized by a relatively low average porosity of 18% with a standard deviation of 3%. The CRIM (Eq. (4)) applied to the permittivity data of GPR cluster 1 yields a very similar porosity of 19 ± 3%. Grain size data and flowmeter measurements suggest that the gravel facies is characterized by a relatively high hydraulic conductivity. The gravel facies is underlain by a well-sorted sand facies (GPR and CPT cluster 2) which is characterized by a relatively high porosity of 29 ± 4% according to CPT water content values and 30 ± 3% according to GPR permittivity data. Grain size based hydraulic conductivity estimates suggest that the sand facies is characterized by a relatively low hydraulic conductivity. Flowmeter measurements suggest that the hydraulic conductivity of the sand facies is relatively low in average but may include significant inhomogeneities. In the left part of the aquifer cross-section, the sand forms an approximately 1.5 m thick horizontal layer. In the right part of the cross-section, this layer decomposes into disconnected lenses, which are only a few decimeters thick. The sand facies is underlain or surrounded by a sandy gravel or gravelly sand facies (GPR and CPT cluster 3) for which CPT and GPR data give an average porosity of 25 ± 3% and 26 ± 2%, respectively.

It is interesting to note that in contrast to full-waveform inversion results at other sites, where a positive correlation between porosity and hydraulic conductivity was observed (Klotzsche et al., 2013), here, our results suggest a negative correlation between porosity and hydraulic conductivity. The reason for this is probably that the high-porosity sand facies has a relatively narrow pore structure, whereas the low-porosity gravel facies has larger individual pores which compensate for the lower total porosity and lead to a higher hydraulic conductivity of the gravel facies compared to the sand facies. This shows that the relationship between porosity and hydraulic conductivity is site dependent, and it shows how important it is to combine complementary investigation tools for aquifer characterization. Based on the GPR inversion results alone, one would probably have assumed (following the findings of Klotzsche et al. (2013)) that the high permittivity zone represents the highest hydraulic conductivity in the aquifer. Instead, flowmeter and grain size data revealed that it is actually the low permittivity zone which can be expected to have the highest hydraulic conductivity at Krauthausen.

Another point we want to note is that the clustered GPR transect shows the spatial connectivity of the individual facies. This makes it possible, for instance, to identify the well connected gravel layer between 3 and 4 m depth or the disconnected sand lenses in the right part of the transect (Fig. 8). As mentioned earlier, identifying connected structures in the subsurface and mapping their spatial distribution is highly valuable for aquifer characterization because connected structures can have a substantial impact on flow and transport (e.g. Bianchi et al., 2011; Zheng et al., 2011). Full-waveform inversion of crosshole GPR data followed by cluster analysis seems to provide an applicable approach to characterize the lateral connectivity of subsurface facies in aquifers, which is difficult to achieve with traditional aquifer exploration techniques.

4. Conclusions

Crosshole ground penetrating radar (GPR) data, acquired along a transect of 20 m length and 10 m depth, were used to characterize the heterogeneous architecture of an alluvial aquifer. Full-waveform inversion of the GPR data yielded the spatial distribution of permittivity and electrical conductivity at the scale of decimeters. Comparison of GPR porosity estimates with co-located CPT porosity logs showed good agreement and gave a linear correlation coefficient of 0.8 and a regression line close to the 1:1 line. Comparison of electrical conductivity data derived from GPR and CPT gave a linear correlation coefficient of 0.67 and a regression line with a slope close to 1, but with a distinct nonzero intercept, caused by an offset in the absolute electrical conductivity values derived from GPR and CPT. The offset could be caused by the inherent differences of the two methods or by biased electrical conductivity starting models used in the GPR full-waveform inversion. Irrespective of the discrepancies in absolute values, we found that GPR and CPT gave relatively consistent results regarding the spatial variations in electrical conductivity.

Cluster analysis of the bivariate GPR inversion results defined three different facies in the aquifer cross-section. The number of facies was confirmed by the results of a cluster analysis conducted (independently) with multivariate CPT data. Moreover, the spatial distribution of facies in CPT profiles showed a good match with the spatial distribution of facies in the GPR transect, which suggests that GPR and CPT identified the same facies in the subsurface. Comparison of the facies distribution with co-located profiles from grain size analyses and flowmeter measurements showed that the derived facies boundaries correlate with changes in grain size and porosity, and to a lesser extent with changes in hydraulic conductivity.

In conclusion, our data suggest that full-waveform inversion of crosshole GPR data followed by cluster analysis is an applicable approach to identify hydrogeological facies and to map their detailed spatial distribution. A particular benefit of using GPR tomographic data is that it yields information about the subsurface on full two-dimensional cross-sections, which makes it possible to assess the spatial connectivity of subsurface structures. Such information is highly valuable for constraining the heterogeneity of stochastic models and can be used to construct geologically realistic aquifer models for numerical flow and transport predictions. Finally, our work shows the benefit of using complementary investigation tools for aquifer characterization. While the GPR data yielded detailed maps of the facies distribution in the aquifer, CPT, grain size and flowmeter data provided the basis for a hydrogeological interpretation of the obtained facies maps.

Acknowledgements

This work was supported in part by the "TERrestrial ENvironmental Observatories" (TERENO) and in part by the "Transregional Collaborative Research Centre 32" (TR32) "Patterns in Soil-Vegetation-Atmosphere Systems: Monitoring, Modelling, and Data Assimilation". We are grateful to Carly Hyatt, whose assistance during the field measurements is highly

appreciated. We want to thank Niklas Linde, Joseph Doetsch and the anonymous reviewer for their constructive suggestions.

References

Anderson, M., 1989. Hydrogeologic facies models to delineate large-scale spatial trends in glacial and glaciofluvial sediments. Geol. Soc. Am. Bull. 101 (4), 501–511.

Anderson-Mayes, A.M., 2002. Strategies to improve information extraction from multivariate geophysical data suites. Explor. Geophys. 33, 57–64.

Barrash, W., Clemo, T., 2002. Hierarchical geostatistics and multifacies systems: Boise hydrogeophysical research site, Boise, Idaho. Water Resour. Res. 38 (10). http://dx.doi.org/10.1029/2002WR001436.

Bayer, P., Huggenberger, P., Renard, P., Comunian, A., 2011. Three-dimensional high resolution fluvio-glacial aquifer analog: Part 1: field study. J. Hydrol. 405 (1–2), 1–9. http://dx.doi.org/10.1016/j.jhydrol.2011.03.038.

Belina, F., Ernst, J., Holliger, K., 2009. Inversion of crosshole seismic data in heterogeneous environments: comparison of waveform and ray-based approaches. J. Appl. Geophys. 68 (1), 85–94. http://dx.doi.org/10.1016/j.jappgeo.2008.10.012.

Bialas, Z., Kleczkowski, A.S., 1970. Über den praktischen Gebrauch von einigen empirischen Formeln zur Berechnung des Durchlässigkeitskoeffzienten. K. Archivum Hydrotechniki, Warschau.

Bianchi, M., Zheng, C., Wilson, C., Tick, G.R., Liu, G., Gorelick, S.M., 2011. Spatial connectivity in a highly heterogeneous aquifer: from cores to preferential flow paths. Water Resour. Res. 47 (5). http://dx.doi.org/10.1029/2009WR008966.

Birchak, J., Gardner, C., Hipp, J., Victor, J., 1974. High dielectric-constant microwave probes for sensing soil-moisture. Proc. IEEE 62 (1), 93–98. http://dx.doi.org/10.1109/PROC.1974.9388.

Bleistein, N., 1986. 2–1/2 dimensional inplane wave-propagation. Geophys. Prospect. 34 (5), 686–703. http://dx.doi.org/10.1111/j.1365-2478.1986.tb00488.x.

Brovelli, A., Cassiani, G., 2008. Effective permittivity of porous media: a critical analysis of the complex refractive index model. Geophys. Prospect. 56 (5), 715–727. http://dx.doi.org/10.1111/j.1365-2478.2008.00724.x.

Brown, W., 1956. Dielectrics. In: Encyclopedia of Physics, vol. 17. Springer Verlag, New York.

Busch, S., van der Kruk, J., Bikowski, J., Vereecken, H., 2012. Quantitative conductivity and permittivity estimation using full-waveform inversion of on-ground GPR data. Geophysics 77 (6), H79–H91. http://dx.doi.org/10.1190/geo2012-0045.1.

Calinski, T., Harabasz, J., 1974. A dendrite method for cluster analysis. Commun. Stat. 3, 1–27.

Carmichael, R.S., 1982. Handbook of Physical Properties of Rocks. CRC Press, Boca Raton, Florida.

Comunian, A., Renard, P., Straubhaar, J., Bayer, P., 2011. Three-dimensional high resolution fluvio-glacial aquifer analog – Part 2: geostatistical modeling. J. Hydrol. 405 (1–2), 10–23. http://dx.doi.org/10.1016/j.jhydrol.2011.03.037.

Dagan, G., 1989. Flow and Transport in Porous Formations. Springer Verlag.

Davis, J.L., Annan, A.P., 1989. Ground-penetrating radar for high-resolution mapping of soil and rock stratigraphy. Geophys. Prospect. 37, 531–551.

Dietrich, P., Tronicke, J., 2009. Integrated analysis and interpretation of cross-hole P- and S-wave tomograms: a case study. Near Surf. Geophys. 7 (2), 101–109.

Dietrich, P., Fechner, T., Whittaker, J., Teutsch, G., 1998. An integrated hydrogeophysical approach to subsurface characterization, In: Herbert, M., Kovar, K. (Eds.), Groundwater Quality: Remediation and Protection. IAHS Publication no. 250, Wallingford, UK, pp. 513–519.

Dobson, M., Ulaby, F., Hallikainen, M., Elrayes, M., 1985. Microwave dielectric behavior of wet soil - Part II: Dielectric mixing models. IEEE Trans. Geosci. Remote Sens. 23 (1), 35–46. http://dx.doi.org/10.1109/TGRS.1985.289498.

Doetsch, J., Linde, N., Coscia, I., Greenhalgh, S.A., Green, A.G., 2010. Zonation for 3D aquifer characterization based on joint inversions of multimethod crosshole geophysical data. Geophysics 75, G53–G64. http://dx.doi.org/10.1190/1.3496476.

Döring, U., 1997. Transport der reaktiven Stoffe Eosin, Uranin und Lithium in einem heterogenen Grundwasserleiter, Ph.D. thesis, Christian Albrecht Universität Kiel.

Eisenberg, D.S., Kauzmann, W., 1969. The Structure and Properties of Water. Oxford University Press.

Englert, A., 2003. Measurement, Estimation and Modelling of Groundwater Flow Velocity at Krauthausen Test Site, Ph.D. Thesis, RWTH Aachen.

Ernst, J.R., Maurer, H., Green, A.G., Holliger, K., 2007a. Full-waveform inversion of crosshole radar data based on 2-D finite-difference time-domain solutions of Maxwell's equations. IEEE Trans. Geosci. Remote Sens. 45 (9), 2807–2828. http://dx.doi.org/10.1109/TGRS.2007.901048.

Ernst, J.R., Green, A.G., Maurer, H., Holliger, K., 2007b. Application of a new 2D time-domain full-waveform inversion scheme to crosshole radar data. Geophysics 72 (5), J53–J64. http://dx.doi.org/10.1190/1.2761848.

Ester, M., Kriegel, H.-P., Sander, J., Xu, X., 1996. A density-based algorithm for discovering clusters in large spatial databases with noise, In: Proc. 2nd Int. Conf. on Knowledge Discovery and Data Mining, Portland, OR, pp. 226–231. Available from: <http://www.aaai.org/Papers/KDD/1996/KDD96-037>.

Everitt, B., Landau, S., Leese, M., 2001. Cluster Analysis. A Hodder Arnold Publication, Wiley.

Feyen, L., Caers, J., 2006. Quantifying geological uncertainty for flow and transport modeling in multi-modal heterogeneous formations. Adv. Water Resour. 29 (6), 912–929. http://dx.doi.org/10.1016/j.advwatres.2005.08.002.

Fogg, G.E., 1986. Groundwater flow and sand body interconnectedness in a thick, multiple-aquifer system. Water Resour. Res. 22 (5), 679–694. http://dx.doi.org/10.1029/WR022i005p00679.

Haendel, F., Dietrich, P., 2012. Relevance of deterministic structures for modeling of transport: the Lauswiesen case study. Ground Water 50 (6), 935–942. http://dx.doi.org/10.1111/j.1745-6584.2012.00948.x.

Holliger, K., Musil, M., Maurer, H., 2001. Ray-based amplitude tomography for crosshole georadar data: a numerical assessment. J. Appl. Geophys. 47 (3–4), 285–298. http://dx.doi.org/10.1016/S0926-9851(01)00072-6.

Huysmans, M., Dassargues, A., 2009. Application of multiple-point geostatistics on modelling groundwater flow and transport in a cross-bedded aquifer (Belgium). Hydrogeol. J. 17 (8), 1901–1911. http://dx.doi.org/10.1007/s10040-009-0495-2.

Huysmans, M., Peeters, L., Moermans, G., Dassargues, A., 2008. Relating small-scale sedimentary structures and permeability in a cross-bedded aquifer. J. Hydrol. 361 (1–2), 41–51. http://dx.doi.org/10.1016/j.jhydrol.2008.07.047.

Isaaks, E.H., Srivastava, M.R., 1990. An Introduction to Applied Geostatistics. Oxford University Press, USA.

Javandel, I., Witherspoon, P.A., 1969. A method of analyzing transient fluid flow in multilayered aquifer. Water Resour. Res. 5 (4), 856–869.

Kemna, A., Vanderborght, J., Kulessa, B., Vereecken, H., 2002. Imaging and characterisation of subsurface solute transport using electrical resistivity tomography (ERT) and equivalent transport models. J. Hydrol. 267, 125–146.

Klotzsche, A., van der Kruk, J., Meles, G.A., Doetsch, J., Maurer, H., Linde, N., 2010. Full-waveform inversion of cross-hole ground-penetrating radar data to characterize a gravel aquifer close to the Thur River, Switzerland. Near Surf. Geophys., 635–649 http://dx.doi.org/10.3997/1873-0604.2010054.

Klotzsche, A., van der Kruk, J., Meles, G.A., Vereecken, H., 2012. Crosshole GPR full-waveform inversion of waveguides acting as preferential flow paths within aquifer systems. Geophysics 77 (4), H57. http://dx.doi.org/10.1190/geo2011-0458.1.

Klotzsche, A., van der Kruk, J., Linde, N., Doetsch, J., Vereecken, H., 2013. 3-D characterization of high-permeability zones in a gravel aquifer using 2-D crosshole GPR full-waveform inversion and waveguide detection. Geophys. J. Int. 195 (2), 932–944. http://dx.doi.org/10.1093/gji/ggt275.

Klotzsche, A., van der Kruk, J., Bradford, J., Vereecken, H., 2014. Detection of spatially limited high-porosity layers using crosshole GPR signal analysis and full-waveform inversion. Water Resour. Res. 50. http://dx.doi.org/10.1002/2013WR015177.

Knudby, C., Carrera, J., 2006. On the use of apparent hydraulic diffusivity as an indicator of connectivity. J. Hydrol. 329 (3–4), 377–389. http://dx.doi.org/10.1016/j.jhydrol.2006.02.026.

Koltermann, C.E., Gorelick, S.M., 1996. Heterogeneity in sedimentary deposits: a review of structure-imitating, process- imitating, and descriptive approaches. Water Resour. Res. 32 (9), 2617–2658.

Li, W., Englert, A., Cirpka, O., Vanderborght, J., Vereecken, H., 2007. Two-dimensional characterization of hydraulic heterogeneity by multiple pumping tests. Water Resour. Res. 43 (4). http://dx.doi.org/10.1029/2006WR005333.

Li, W., Englert, A., Cirpka, O., Vereecken, H., 2008. Three-dimensional geostatistical inversion of flowmeter and pumping test data. Ground Water 46 (2), 193–201. http://dx.doi.org/10.1111/j.1745-6584.2007.00419.x.

Linde, N., Binley, A., Tryggvason, A., Pedersen, L.B., Revil, A., 2006. Improved hydrogeophysical characterization using joint inversion of cross-hole electrical resistance and ground-penetrating radar traveltime data. Water Resour. Res. 42 (12). http://dx.doi.org/10.1029/2006WR005131.

MacKay, D., 2002. Information Theory, Inference & Learning Algorithms. Cambridge University Press, USA.

MacQueen, J.B., 1967. Some methods for classification and analysis of multivariate observations. In: Cam, L.M.L., Neyman, J. (Eds.), Proceedings of the Fifth Berkeley Symposium on Mathematical Statistics and Probability, vol. 1, University of California Press, pp. 281–297.

Maurer, H., Musil, M., 2004. Effects and removal of systematic errors in crosshole georadar attenuation tomography. J. Appl. Geophys. 55 (3–4), 261–270. http://dx.doi.org/10.1016/j.jappgeo.2004.02.003.

Meles, G.A., van der Kruk, J., Greenhalgh, S.A., Ernst, J.R., Maurer, H., Green, A.G., 2010. A new vector waveform inversion algorithm for simultaneous updating of conductivity and permittivity parameters from combination Crosshole/Borehole-to-surface GPR data. IEEE Trans. Geosci. Remote Sens. 48 (12), 4329. http://dx.doi.org/10.1109/TGRS.2010.2090010.

Meles, G.A., Greenhalgh, S.A., van der Kruk, J., Green, A.G., Maurer, H., 2011. Taming the non-linearity problem in GPR full-waveform inversion for high contrast media. J. Appl. Geophys. 73, 174–186.

Miall, A., 1985. Architectural-element analysis: a new method of facies analysis applied to fluvial deposits. Earth Sci. Rev. 22 (4), 261–308, http://dx.doi.org/10.1016/0012-8252(85)90001-7.

Miall, A., 1996. The Geology of Fluvial Deposits. Springer Verlag.

Molz, F., Morin, R.H., Hess, A.E., Melville, J.G., Goven, O., 1989. The impeller meter for measuring aquifer permeability variations: evaluation and comparison with tests. Water Resour. Res. 25 (7), 1677–1686.

Molz, F., Boman, G.K., Young, S.C., Waldrop, W.R., 1994. Borehole flowmeters: field application and data analysis. J. Hydrol. 163, 347–371.

Müller, K., Vanderborght, J., Englert, A., Kemna, A., Huisman, J., Rings, J., Vereecken, H., 2010. Imaging and characterization of solute transport during two tracer tests in a shallow aquifer using electrical resistivity tomography and multilevel

groundwater samplers. Water Resour. Res. 46 (3). http://dx.doi.org/10.1029/2008WR007595.

Oberröhrmann, M., Klotzsche, A., Vereecken, H., van der Kruk, J., 2013. Optimization of acquisition setup for cross-hole GPR full-waveform inversion using checkerboard analysis. Near Surf. Geophys. 11 (2, SI), 197–209. http://dx.doi.org/10.3997/1873 0604.2012045.

Paasche, H., Tronicke, J., Dietrich, P., 2010. Automated integration of partially collocated models: subsurface zonation using a modified fuzzy c-means cluster analysis algorithm. Geophysics 75, P11–P22.

Paasche, H., Tronicke, J., Dietrich, P., 2012. Zonal cooperative inversion of partially co-located data sets constrained by structural a priori information. Near Surf. Geophys. 10, 103–116.

Renard, P., Allard, D., 2013. Connectivity metrics for subsurface flow and transport. Adv. Water Resour. 51, 168–196. http://dx.doi.org/10.1016/j.advwatres.2011.12.001.

Riva, M., Guadagnini, L., Guadagnini, A., Ptak, T., Martac, E., 2006. Probabilistic study of well capture zones distribution at the Lauswiesen field site. J. Contam. Hydrol. 88 (1–2), 92–118. http://dx.doi.org/10.1016/j.jconhyd.2006.06.005.

Robinson, D.A., Jones, S.B., Wraith, J.M., Or, D., Friedman, S.P., 2003. A review of advances in dielectric and electrical conductivity measurement in soils using time domain reflectometry. Phys. Rev. 2 (4), 444–475.

Rogiers, B., 2013. Multi-Scale Aquifer Characterization: from Outcrop Analogue, Direct-Push and Borehole Investigations Towards Improved Groundwater Flow Models, PhD thesis, Faculty of Science, KU Leuven, 234 pp. ISBN 978-90-8649-672-3 – D/2013/10.705/87 – ISSN 0250-7803.

Ronayne, M.J., Gorelick, S.M., Caers, J., 2008. Identifying discrete geologic structures that produce anomalous hydraulic response: an inverse modeling approach. Water Resour. Res. 44 (8). http://dx.doi.org/10.1029/2007WR006635.

Roth, K., Schulin, R., Fluhler, H., Attinger, W., 1990. Calibration of time domain reflectometry for water-content measurement using a composite dielectric approach. Water Resour. Res. 26 (10), 2267–2273. http://dx.doi.org/10.1029/90WR01238.

Schneider, M., 1995. Charakterisierung der Variabilität der Permeabilität in einem quartären Grundwasserleiter, Master thesis, Department of Engineering Geology and Hydrogeology, Rheinisch-Westfälischen Technischen Hochschule Aachen, and ICG-4, Forschungszentrum Jülich.

Steelman, C.M., Endres, A.L., 2011. Comparison of petrophysical relationships for soil moisture estimation using GPR ground waves. Phys. Rev. 10 (1), 270–285. http://dx.doi.org/10.2136/vzj2010.0040.

Tillmann, A., Englert, A., Nyari, Z., Fejes, I., Vanderborght, J., Vereecken, H., 2008. Characterization of subsoil heterogeneity, estimation of grain size distribution and hydraulic conductivity at the Krauthausen test site using cone penetration test. J. Contam. Hydrol. 95 (1–2), 57–75. http://dx.doi.org/10.1016/j.jconhyd.2007.07.013.

Topp, G., Davis, J., Annan, A., 1980. Electromagnetic determination of soil-water content – measurements in coaxial transmission-lines. Water Resour. Res. 16 (3), 574–582. http://dx.doi.org/10.1029/WR016i003p00574.

Tronicke, J., Holliger, K., Barrash, W., Knoll, M.D., 2004. Multivariate analysis of cross-hole georadar velocity and attenuation tomograms for aquifer zonation. Water Resour. Res. 40 (1). http://dx.doi.org/10.1029/2003WR002031.

Vanderborght, J., Vereecken, H., 2001. Analyses of locally measured bromide breakthrough curves from a natural gradient tracer experiment at Krauthausen. J. Contam. Hydrol. 48 (1–2), 23–43.

Vereecken, H., Döring, U., Hardelauf, H., Jaekel, U., Hashagen, U., Neuendorf, O., Schwarze, H., Seidemann, R., 2000. Analysis of solute transport in a heterogeneous aquifer: the Krauthausen field experiment. J. Contam. Hydrol. 45, 329–358.

Webb, E., Anderson, M., 1996. Simulation of preferential flow in three-dimensional, heterogeneous conductivity fields with realistic internal architecture. Water Resour. Res. 32 (3), 533–545. http://dx.doi.org/10.1029/95WR03399.

Yang, X., Klotzsche, A., Meles, G., Vereecken, H., van der Kruk, J., 2013. Improvements in crosshole GPR full-waveform inversion and application on data measured at the Boise hydrogeophysics research site. J. Appl. Geophys. 99, 114–124, doi:http://dx.doi.org/10.1016/j.jappgeo.2013.08.007.

Zheng, C., Gorelick, S., 2003. Analysis of solute transport in flow fields influenced by preferential flowpaths at the decimeter scale. Ground Water, 41(2), 142–155, 2001, doi:10.1111/j.1745-6584.2003.tb02578.x, MODFLOW 2001 and Other Modeling Odysseys Conference, COLORADO SCH MINES, GOLDEN, CO, SEP 12-14.

Zheng, C., Bianchi, M., Gorelick, S., 2011. Lessons learned from 25 years of research at the MADE site. Ground Water 49 (5), 649–662. http://dx.doi.org/10.1111/j.1745-6584.2010.00753.x.

Zinn, B., Harvey, C.F., 2003. When good statistical models of aquifer heterogeneity go bad: a comparison of flow, dispersion, and mass transfer in connected and multivariate gaussian hydraulic conductivity fields. Water Resour. Res. 39 (3). http://dx.doi.org/10.1029/2001WR001146.

Update

Journal of Hydrology

Volume 590, Issue , November 2020, Page

DOI: https://doi.org/10.1016/j.jhydrol.2020.125483

Journal of Hydrology 590 (2020) 125483

Contents lists available at ScienceDirect

Journal of Hydrology

journal homepage: www.elsevier.com/locate/jhydrol

Corrigendum to "Imaging and characterization of facies heterogeneity in an alluvial aquifer using GPR full-waveform inversion and cone penetration tests" [J. Hydrol. (2015) 680–695]

N. Gueting[a,*], A. Klotzsche[a,b], J. van der Kruk[a,b], J. Vanderborght[a,b], H. Vereecken[a,b], A. Englert[c]

[a] Agrosphere Institute, IBG-3, Forschungszentrum Jülich GmbH, 52428 Jülich, Germany
[b] Centre for High-Performance Scientific Computing in Terrestrial Systems (TerrSys), Germany
[c] Earth Sciences Department, Ruhr University Bochum, 44801 Bochum, Germany

The authors regret that an error has occurred and the following corrections need to be recorded regarding the above cited paper. After reanalysing the crosshole GPR data, we found an error in the automatic picking routine for estimating the time zero of the GPR data. After correction, the GPR data was shifted in time affecting the calculated permittivities ε_r and electrical conductivities σ (Original Figs. 3 and 4). Using the corrected time zero, the permittivity and conductivity results of the full-waveform inversion were updated. The comparison between the original and correct tomograms now show that the permittivity and electrical conductivity results are approximately 4 higher and 10 mS/m lower, respectively (see Fig. 1). Using this correction the full-waveform inversion results are in a better agreement with the CPT data (Fig. 2). It is Interesting to note that the constant shift of −0.08 that was applied previously to align the porosity CPT data with the FWI results is not

DOI of original article: https://doi.org/10.1016/j.jhydrol.2015.03.030
* Corresponding author.
E-mail addresses: n.gueting@fz-juelich.de (N. Gueting), a.klotzsche@fz-juelich.de (A. Klotzsche).

https://doi.org/10.1016/j.jhydrol.2020.125483

Available online 25 September 2020

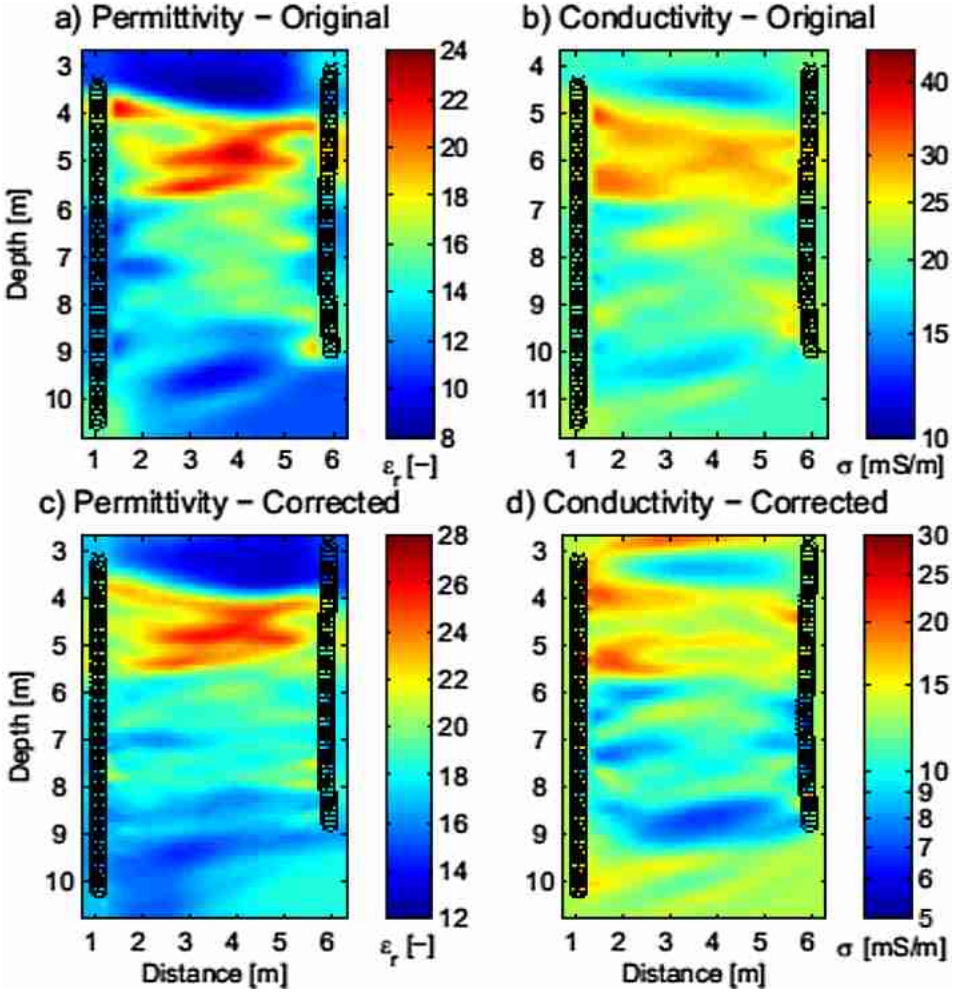

Fig. 1. Comparison for the exemplary transect B38-B31 of the original a) permittivity and b) electrical conductivity full-waveform inversion results, and, the corrected c) permittivity and d) electrical conductivity results using the corrected time zero estimation. Please note the different color scales of the tomograms.

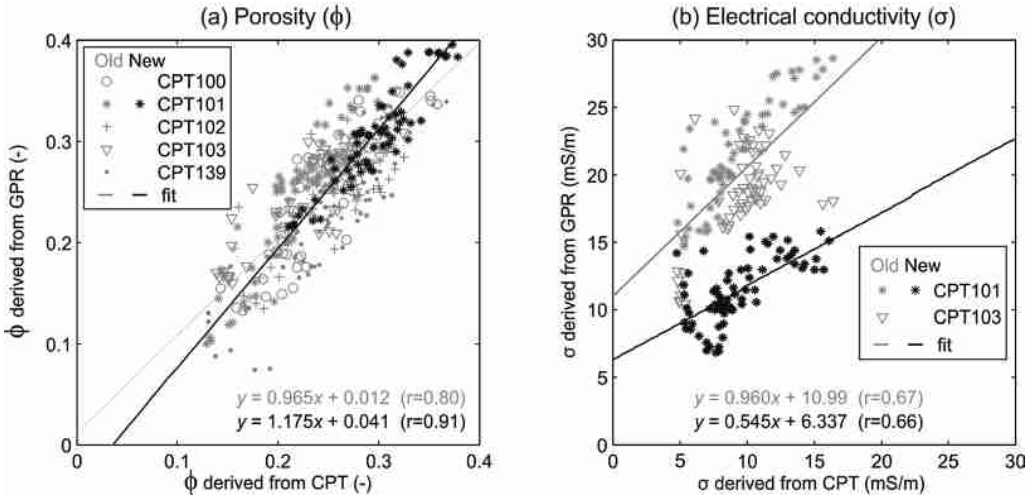

Fig. 2. Comparison of the old (grey) and corrected (black) cross-plots between the FWI results and CPT data. Cross-plots of a) porosities and b) electrical conductivities derived from CPT and GPR data. Results based on the corrected FWI are shown in black for the exemplary transect B38-B31 for which co-located porosity and electrical conductivity data of the CPT 101 exist. Data based on Gueting et al. (2015) presented in grey for the a) five and b) two profiles and corresponding co-located CPT porosity and electrical conductivity data, respectively. Regression lines through all data points are depicted in grey and black for old and corrected data, respectively. The corresponding straight-line equations are given at the bottom of the cross plot, *r* is the correlation coefficient.

necessary anymore. The porosity values based on the updated FWI results are now in a very good agreement with the original values of Tillman et al. (2008) indicated by a correlation coefficient r of 0.91, which was before 0.80 (Fig. 2a). Furthermore, the updated electrical conductivity FWI results are closer to the electrical conductivity results based on the CPT data (Fig. 2b). We expect only minor changes in the results using the cluster analysis to derive the facies of the aquifer indicating that the main conclusions of the paper remain valid. The authors would like to apologise for any inconvenience caused.